

Epoch of Reionisation 21cm Forecasting From MCMC-Constrained Semi-Numerical Models

Sultan Hassan¹, Romeel Davé^{1,2,3}, Kristian Finlator⁴, Mario G. Santos^{1,5}

¹ *University of the Western Cape, Bellville, Cape Town, 7535, South Africa*

² *South African Astronomical Observatories, Observatory, Cape Town, 7925, South Africa*

³ *African Institute for Mathematical Sciences, Muizenberg, Cape Town, 7945, South Africa*

⁴ *New Mexico State University, Las Cruces, NM 88003, United States*

⁵ *SKA SA, The Park, Park Road, Pinelands 7405, South Africa*

20 December 2016

ABSTRACT

The recent low value of Planck (2016) integrated optical depth to Thomson scattering suggests that the reionization occurred fairly suddenly, disfavoring extended reionization scenarios. This will have a significant impact on the 21cm power spectrum. Using a semi-numerical framework, we improve our model from Hassan et al. (2016) to include time-integrated ionisation and recombination effects, and find that this leads to more sudden reionisation. It also yields larger H II bubbles which leads to an order of magnitude more 21cm power on large scales, while suppressing the small scale ionization power. Local fluctuations in the neutral hydrogen density play the dominant role in boosting the 21cm power spectrum on large scales, while recombinations are subdominant. We use a Monte Carlo Markov Chain approach to constrain our model to observations of the star formation rate functions at $z = 6, 7, 8$ from Bouwens et al. (2015), the Planck (2016) optical depth measurements, and the Becker & Bolton (2013) ionising emissivity data at $z \sim 5$. We then use this constrained model to perform 21cm forecasting for LOFAR, HERA, and SKA in order to determine how well such data can characterise the sources driving reionisation. We find that the 21cm power spectrum alone can somewhat constrain the halo mass dependence of ionising sources, the photon escape fraction and ionising amplitude, but combining the 21cm data with other current observations enables us to separately constrain all these parameters. Our framework illustrates how 21cm data can play a key role in understanding the sources and topology of reionisation as observations improve.

Key words: galaxies: evolution - galaxies: formation - galaxies: high-redshift - cosmology: theory - dark ages, reionization, first stars early Universe.

1 INTRODUCTION

The redshifted 21cm line from the Epoch of Reionization (EoR) provides numerous astrophysical and cosmological information about the formation and evolution of the first stars and galaxies (Barkana & Loeb 2001). Many ongoing and forthcoming experiments such as the Low Frequency Array (LOFAR)¹, the Hydrogen Epoch of Reionisation Array (HERA)², and the Square Kilometer Array (SKA-Low)³, are devoted to observing the dense neutral hydrogen gas that traces the cosmic web at redshifts beyond 7, and will likely detect the 21cm power spectrum in the near future. It

is thus important to develop robust and comprehensive theoretical models that can utilise such information, along with observations from many other wavelengths and facilities, in order to optimally constrain the physical processes driving reionisation.

The recent low value of Planck (2016) integrated optical depth to Thomson scattering suggests that the EoR may have occurred more suddenly, and at much later times, than what was previously believed (Hinshaw et al. 2013). This low value of $\tau = 0.058 \pm 0.012$ prefers EoR models with late onset and shorter duration. This, in turn, is expected to have a significant impact on the expected 21cm signal. Proper modelling of the sources and sinks of ionising photons during the EoR is required to accurately model the H II bubbles and study their sizes and distributions. This will

¹ <http://www.lofar.org/>

² <http://reionisation.org>

³ <https://www.skatelescope.org>

allow us to connect the observed 21cm power spectrum with the physical characteristics of the sources and sinks.

There are several major challenges to modeling the EoR and its redshifted 21cm signal which make this a difficult problem. These requirements include: (i) Large volumes (~ 500 Mpc) in order to capture the large scale H I fluctuations that will be in upcoming 21cm observations; (ii) High resolution that is sufficient to resolve the ionizing sources and self-shielding systems in sub-kpc scales (Iliev et al. 2015); (iii) accurately tracking the ionizing radiation and feedback processes from the sub-kpc up to Mpc scales. For these reasons, self-consistently simulating the EoR represents an immense computational challenge that no current model has been able to fully meet.

Nonetheless, great progress has been made in simulating various aspects of the EoR, both on small and large scales. The full radiative transfer simulations (Gnedin (2000, 2014); Pawlik & Schaye (2008); Finlator & Davé (2009); Finlator et al. (2013); Katz et al. (2016)) possess high resolution and are able to propagate the radiation with minimal physical assumption, although they generally cannot capture volumes larger than 20 Mpc while simultaneously treating the contribution of atomically-cooled halos. Post-processed radiative transfer simulations (Razoumov et al (2002); Mellema et al (2006); McQuinn et al (2007); Thomas et al (2009); Iliev et al. (2014); Bauer et al. (2015)) can access larger volumes though they do not account for various feedback effects on galaxies self-consistently. Semi-analytical EoR models (Mitra et al. 2011, 2013) are very successful in studying and constraining the globally averaged astrophysical quantities and parameters during EoR (Mitra et al. 2012, 2015) based on current observations, but the lack of dynamic range prevents them from studying the 21cm fluctuations. Semi-numerical models (Mesinger & Furlanetto (2007); Zahn et al (2007); Choudhury et al (2009); Santos et al. (2010)) based typically on quasi-linear density evolution and coarse modeling of the source population can evolve the EoR on the largest scales, but use highly parameterised approximations for the source and sink populations. Such semi-numerical models nevertheless they have been shown to reproduce similar reionization histories as obtained by radiative transfer simulations (Zahn et al (2011); Majumdar et al. (2014)).

Semi-numerical models are thus ideally suited to studying the large-scale ($\gtrsim 1$ Mpc) 21cm power spectrum that will be measured with upcoming radio facilities. However, there are many uncertainties associated with the semi-numerical method. These include: (1) The relationship between halo mass and ionizing luminosity; (2) The relationship between the large-scale density field and the recombination rate that emerges from small-scale clumping; and (3) The condition for a region to be ionized. While the third uncertainty is purely numerical, the first two provide an opportunity to constrain the astrophysical quantities and parameters based on 21cm and other EoR observations.

In Hassan et al. (2016), we took the approach of marrying high-resolution radiative hydrodynamic simulations with a semi-numerical model in order to gain some advantages of each, in particular enabling greater physical realism into the parameterised source and sink populations required for the semi-numerical approach. To do so, we derived new parametrizations of the ionization rate R_{ion} and recombination rate R_{rec} , as functions of halo mass, overdensity and

redshift, extracted from our high resolution radiative transfer hydrodynamic simulation (Finlator et al. 2015) (hereafter 6/256-RT) and larger hydrodynamic simulation (Davé et al. 2013) (hereafter 32/512). We then implemented these parametrizations into our semi-numerical code SIMFAST21 to identify the ionized regions. This more realistic modeling essentially replaces the canonical efficiency parameter ζ method in previous semi-numerical EoR modeling. We found that the R_{ion} scales super-linearly with halo mass ($R_{\text{ion}} \propto M_h^{1.4}$) in contrast to the typically assumed linear relationship between the efficiency parameter ζ and halo mass. We showed that using these new parametrizations (R_{ion} and R_{rec}) allows us to simultaneously match various EoR key observables with a relatively low escape fraction, independent of halo mass and redshift. We also found that the R_{ion} boosts the small scale 21cm power spectrum while R_{rec} suppresses the 21cm power on large scales during cosmic reionizations.

Hassan et al. (2016) thus improved upon the first two major uncertainties in semi-numerical models, namely the ionisation and recombinations. However, this work still assumed an ionization condition based on the *instantaneous* balance between ionisations and recombinations – in other words, if there were instantaneously more ionisations than recombinations, that volume of space was considered fully ionised. However, this is not physically fully accurate, since the excess ionising photons in such regions would still require some time to fully ionise the hydrogen in that region. The instantaneous criterion also ignores partial ionizations, effectively throwing away ionising photons. In the limiting case where reionisation proceeds quickly, this is perhaps not a bad approximation, but ideally we aim to relax this instantaneous assumption. In essence, it is likely that our ionisations were too efficient, which can affect the topology and duration of the EoR.

In this paper, we improve upon our previous ionization condition by tracking the actual number of neutral hydrogen atoms, ionising photons, and recombinations. This leads to a time dependent ionization condition that is analogous to the well-known ionisation balance equation. With this, it turns out that reionisation occurs more suddenly, as preferred by the recent Planck (2016) constraints. We compare this to our previous Instantaneous EoR model Hassan et al. (2016) in terms of their H II bubble sizes, EoR history, and 21cm power spectra.

Another aspect for improvement is in parameter constraints. In Hassan et al. (2016), we constrained to observations essentially by eye, since we only had one free parameter, namely the escape fraction of ionising photons. However, here we would like to relax the assumptions of R_{ion} that we were previously simply taking from the high-resolution hydrodynamic simulations, and instead constrain the source population characteristics directly from data. We thus consider a generalised model with three free parameters: the escape photon fraction f_{esc} , the ionising emissivity amplitude A_{ion} (R_{ion} amplitude), and the ionising emissivity-halo mass power dependence C_{ion} ($R_{\text{ion}} \propto M_h^{C_{\text{ion}}}$ non-linear power). We then perform a Bayesian Monte Carlo Markov Chain (MCMC) search in order to constrain these free parameters against various EoR observations. We also determine how these parameter constraints will be improved by upcoming 21cm observations, thereby providing forecasting for the ongoing and future EoR experiments LOFAR, HERA,

and SKA-Low. By including constraints from all such observations, we thus determine how well we can constrain the EoR source population as characterised by our three free parameters.

This paper is organized as follows: In section 2, we introduce our previous Instantaneous EoR model and our new Time-integrated model. We study and compare these models' impacts on various EoR observables including the 21cm power spectrum in section 3. In section 4, we create several EoR models to study their effects on the 21cm power spectrum. In section 5, we calibrate the Time-integrated model to various EoR observations. We perform the 21cm forecasting in section 6 and draw our concluding remarks in section 7.

Throughout this work, we adopt a Λ CDM cosmology in which $\Omega_M = 0.3$, $\Omega_\Lambda = 0.7$, $h \equiv H_0/(100 \text{ km/s/Mpc}) = 0.7$, a primordial power spectrum index $n = 0.96$, an amplitude of the mass fluctuations scaled to $\sigma_8 = 0.8$, and $\Omega_b = 0.045$. We quote all results in comoving units, unless otherwise stated.

2 SIMULATIONS

We use a semi-numerical code SIMFAST21 (Santos et al. 2010), which we briefly review here. SIMFAST21 simulation begins by generating the density field from a Gaussian distribution using a Monte-Carlo approach. The generated density field will then be dynamically evolved from linear to non-linear regime by applying the Zel'Dovich (1970) approximations. The dark matter halos are generated using the well-known excursion-set formalism. In the standard SIMFAST21, the ionized regions are identified using a similar form of the excursion-set formalism, which is based on a constant efficiency parameter ζ . In the original SIMFAST21 code, the ionisation condition simply compares the amount of collapsed dark matter halo f_{coll} to the efficiency parameter ζ – any region will be flagged as ionised if:

$$f_{\text{coll}} \geq \zeta^{-1}. \quad (1)$$

The efficiency parameter ζ is a model free parameter which can be tuned to match some observations. This condition generates the ionization field, which may be used along with the density field to obtain the 21cm brightness temperature. We refer the reader to Santos et al. (2010) for more details on this model and the code algorithm.

We now describe our two extensions to SIMFAST21. The first was presented in Hassan et al. (2016), which we review next, and incorporates the ionisation and recombination rate parameterisations taken from hydrodynamic simulations, but utilises an instantaneous ionisation condition. We then describe our further extension here in order to improve the ionisation condition by tracking the neutral fraction in a time-integrated manner. We will call this the “Instantaneous ionisation” and “Time-integrated ionisation” models.

2.1 Instantaneous ionisation model

As described in Hassan et al. (2016), here we replace the efficiency parameter ζ with direct parameterisations of the ionization rate R_{ion} and recombination rate R_{rec} as functions of halo mass M_h , overdensity Δ , and redshift z , taken

from our 6/256-RT and 32/512 simulations. Our best-fit non-linear ionization rate R_{ion} parametrization takes the following form:

$$\frac{R_{\text{ion}}}{M_h} = A_{\text{ion}} (1+z)^{D_{\text{ion}}} (M_h/B_{\text{ion}})^{C_{\text{ion}}} \exp(-(B_{\text{ion}}/M_h)^{3.0}), \quad (2)$$

where $A_{\text{ion}} = 1.08 \times 10^{40} \text{ M}_\odot^{-1} \text{ s}^{-1}$, $B_{\text{ion}} = 9.51 \times 10^7 \text{ M}_\odot$, $C_{\text{ion}} = 0.41$ and $D_{\text{ion}} = 2.28$. Meanwhile, we parameterise the recombination rate as:

$$\frac{R_{\text{rec}}}{V} = A_{\text{rec}} (1+z)^{D_{\text{rec}}} \left[\frac{(\Delta/B_{\text{rec}})^{C_{\text{rec}}}}{1 + (\Delta/B_{\text{rec}})^{C_{\text{rec}}}} \right]^4, \quad (3)$$

where $A_{\text{rec}} = 9.85 \times 10^{-24} \text{ cm}^{-3} \text{ s}^{-1}$, $B_{\text{rec}} = 1.76$, $C_{\text{rec}} = 0.82$, $D_{\text{rec}} = 5.07$.

Our ionisation condition is taken to be

$$f_{\text{esc}} R_{\text{ion}}(M_h, z) \geq R_{\text{rec}}(\Delta, z), \quad (4)$$

where f_{esc} is the escape photon fraction; cells satisfying this criterion are considered fully ionised, otherwise they are fully neutral.

Using this model, it has been shown in Hassan et al. (2016) that one can match simultaneously several EoR key observables, such as Planck (2015) optical depth, Becker & Bolton (2013) ionizing emissivity and Fan et al (2006) filling factor measurement, by only a constant $f_{\text{esc}} = 4-6\%$ independent of halo mass or redshift. We refer the reader to Hassan et al. (2016) for more details about the model and these new parametrizations.

2.2 Time-integrated ionisation model

The model in Hassan et al. (2016) (our Instantaneous EoR model) has several drawbacks. First, the ionization condition, equation (4), is an instantaneous criterion which compares the escaped ionization rate $f_{\text{esc}} R_{\text{ion}}$ with the recombination rate R_{rec} , instead of comparing the actual numbers of ionising photons to that of recombinations. Second, the ionization condition, equation (4), assumes maximum recombination rate R_{rec} from all cells/regions as they were fully ionised.

To improve on these, we modify the ionisation condition to account for the evolving neutral hydrogen fraction, which allows us to account for the existing number of hydrogen atoms in each region as well as to compute the recombination based on the current ionised fraction. Hence we now employ a time dependent integral ionisation condition:

$$f_{\text{esc}} R_{\text{ion},V} \geq x_{\text{HII}} R_{\text{rec},V} + (1 - x_{\text{HII}}) N_{\text{H}}, \quad (5)$$

where

$$R_{\text{ion},V} = \int_{\text{dn}} \int_V \frac{dn}{dM} R_{\text{ion}}(M_h, z) dM dV dt,$$

and

$$R_{\text{rec},V} = \int_V R_{\text{rec}}(\Delta, z) dV dt.$$

All of above quantities are defined within the spherical region volume (V) specified by the excursion set-formalism. For a given volume V , the x_{HII} is the ionization fraction, n is the number density of halos, N_{H} is the total number of hydrogen, the R_{ion} is the total number of ionising photons

from all sources being emitted in time interval dt , and N_{rec} is the maximum number of recombinations during that time.

The left hand side (LHS) of our new ionization condition (eq. 5) represents the actual number of escaped ionising photons being emitted in dt . The first term of the right hand side (RHS) of this condition is the actual number of recombinations occurring during dt in regions with an ionization fraction of x_{HII} . This term then tracks the exact number of recombinations even from partially ionised regions with $0 < x_{\text{HII}} < 1$. This recombination term has no effect at early times of EoR when the universe is completely neutral, but becomes the dominant sink for ionising photons at late stages of the EoR (Sobacchi & Mesinger 2014).

The second term of the RHS of equation (5) denotes the total number of neutral hydrogen in the simulation box. At early EoR stages, the escaped ionising photons (LHS) fights only with the neutral hydrogen term $(1 - x_{\text{HII}})N_{\text{H}}$. As the EoR proceeds, the neutral hydrogen term becomes less significant, and the recombinations start to play the leading role in forestalling reionisation. Hence this provides a more physically motivated ionization condition, in a similar form to the standard ionization balance equation.

The condition is clearly time-dependent, unlike the Instantaneous ionisation model for which the ionisation condition could be evaluated independently at each time-step. Thus our new scheme can be sensitive to the choice of the time-step dt used to perform the integration. For instance, a larger $dt(dz)$ will result in more ionising photons and also more recombinations. This then leads to a wrong evolving ionization balance. We have conducted convergence tests to determine that $dz = 0.125$ provides a numerically-converged answer to within 0.01%. Our new method thus requires higher computational expenses to evolve the ionisation state forward. We will explore possible variations of the ionisation condition from equation (5) in §4, to study their impact on the 21cm power spectrum.

It turns out, as we will show, that the instantaneous ionisation condition results in more extended reionisation history, while our new time-integrated condition yields more sudden reionisation. Next, we will investigate their differences in terms of the EoR history, topology, and the 21cm power spectrum.

3 IMPACTS ON THE EOR OBSERVABLES

We use the Full model in Hassan et al. (2016) as our fiducial “Instantaneous” reionisation model. This model uses equation(4) to identify the ionized regions with $f_{\text{esc}} = 4\%$ in a large volume box of $L = 300$ Mpc and a number of cells $N = 560^3$. We have shown that this model matches various observations of the EoR including the Planck (2015) optical depth $\tau = 0.066$. Using the same density field boxes and halo catalogues, we run our new Time-integrated reionisation model with parameters calibrated against various EoR key observations (see section 5), including the new Planck (2016) optical depth. The two models are tuned to different τ_e values, but we do our 21cm comparison at a given neutral fraction since it has been shown that the 21cm power spectrum shape is more sensitive to the neutral fraction (e.g. see Zahn et al (2007); Mesinger & Furlanetto (2007)). We thus begin by comparing the Instantaneous and Time-integrated

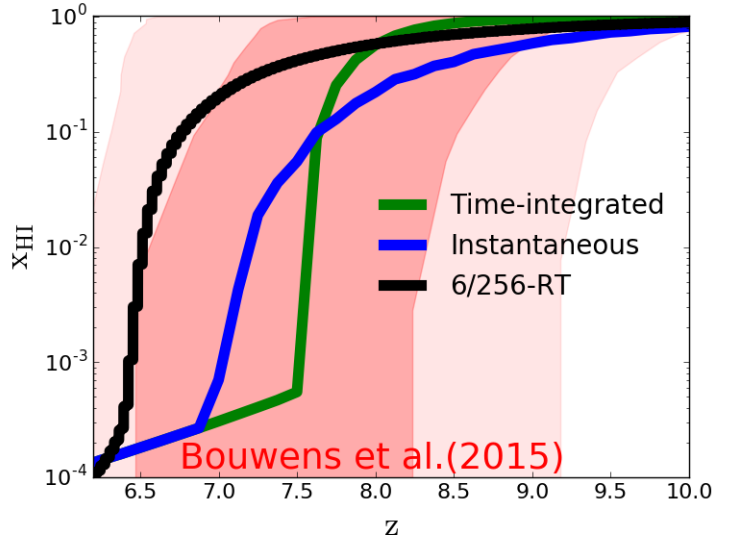


Figure 1. The volume-weighted average neutral fraction evolution as a function of redshift. The Time-integrated EoR model, the Instantaneous EoR model developed in Hassan et al. (2016), and the 6/256-RT simulation are represented by the green, blue, black lines, respectively. The shaded areas are several quasars and Ly- α constraints as compiled by Bouwens et al. (2015). It is quite clear that all models are consistent with the observational constraints by Bouwens et al. (2015). Differences between models are explained in the text.

models’ differences in terms of their global neutral fraction history.

3.1 EoR ionisation history

Figure 1 shows the global reionisation history produced by our two fiducial models, Instantaneous and Time-integrated, compared to the neutral fraction constraints obtained by Bouwens et al. (2015) via a compilation from various observables. We immediately see that the green line showing the new time-integrated ionisation condition shows a more sudden transition from fully ionised to fully neutral. Meanwhile, the blue line from our old instantaneous condition results in a more extended reionisation epoch. Nonetheless, in both cases, reionization occurs in our two models within observational constraints (light-red shaded areas). It is perhaps worth noting that, unlike a few years ago when the canonical redshift for the end of reionisation was regarded as $z \sim 6$, current constraints from both observations and models favors the end of reionisation to occur at $z \sim 7$ or perhaps a bit higher.

This plot already shows that accounting for the neutral gas through comparing the number of neutral atoms and ionising photons (equation (5)) versus comparing instantaneous rates (equation (4)) has a significant impact on the reionization history. The Time-integrated model is qualitatively more compatible with the picture that has been suggested by recent Planck (2016) constraints that favours sudden EoR scenarios. We emphasize the fact that if we tune the Time-integrated model optical depth to match the Instantaneous model optical depth ($\tau = 0.066$, Planck (2015)), the Time-integrated model will require higher f_{esc} and shift

reionization towards higher redshifts, but nevertheless the reionization history shape will remain sudden as shown later in figure 9. We will come back to this point later in §5.2.2.

From figure 1, we also see that both models Instantaneous and Time-integrated reionize the universe earlier than the 6/256-RT simulation. As discussed before in Hassan et al. (2016), the small box size ($6 \text{ h}^{-1} \text{ Mpc}$) of 6/256-RT does not capture the large scale fluctuations that give rise to the most massive halos that provide a significant fraction of reionising photons. Hence at a fixed optical depth, it is expected that the 6/256-RT might reionize the universe much later than the Time-integrated model due to the box size limitations.

An informative way to examine these models is by viewing light cones, as shown in Figure 2. These have been constructed by projecting the ionisation state within the simulation volume along a specific line-of-sight, evolving with redshift. Figure 2 confirms that our previous model (the Full model of Hassan et al. 2016) produces a more extended EoR scenario that corresponds to an early onset and a very late end with a duration of $\Delta z \sim 10$. Unlike the Instantaneous model, figure 2 also shows that our new model (equation (5)) yields a sudden reionization scenario where the EoR starts very late (once $x_{\text{HI}} < 1.0$) and ends (when x_{HI} drops below 10^{-3}) very quickly within a duration of $\Delta z \sim 4$. More strikingly, it also shows that the Time-integrated EoR model produces larger ionized bubbles while the Instantaneous model yields many ionized bubbles of smaller sizes. This can further be quantified by studying their differences in terms of the ionization field power spectra.

3.2 EoR topology

It is useful to compare the models at a specific neutral fraction, since this best illustrates the difference in topology. Figure 3 compares our Instantaneous and Time-integrated models in terms of their ionization maps when the EoR is half-way through, i.e. with a globally-averaged $x_{\text{HI}} \sim 0.5$. These ionization maps show the spatial distribution of the large and small ionised bubbles (black regions) over 300 Mpc scales. From Figure 3, we see that the Instantaneous model produces many small H II bubbles more uniformly distributed across the ionization map. This shows that the EoR in the Instantaneous model proceeds from small scales, and the ionising photons are able to reionise locally everywhere. This is because the instantaneous ionisation rate can easily exceed the recombination rate (see equation (4)) on small scales when neglecting the local neutral hydrogen content.

In contrast, the Time-integrated model ionization map shows very large H II bubbles. This may be explained by interpreting the Time-integrated model ionization condition (equation (5)). As noted earlier, at high redshifts when the universe is neutral ($x_{\text{HI}} \sim 0$), the recombination term can be neglected. In this case, the Time-integrated model only compares the escaped ionising photons with the total number of neutral hydrogen atoms. This condition dominates until the region becomes partially ionised. At that point, recombinations will start to occur because of the nonzero ionisation fraction x_{HI} , but still this region is now less neutral, which will allow more rapid ionisation. However, different forms of ionization condition yield very different HI fluctuations (see §4). In general, the sources and sinks are

occurring within the regions that are densest and thus contain the most number of neutral hydrogen atoms. The high density causes the ionising photons to be ineffective at ionising local regions, until such time as significant ionisations happen, which then rapidly ionise the surrounding regions.

Figure 4 shows the ionization field power spectra of our fiducial models at different stages of reionization when the universe is 25%, 50% and 75% reionized. These neutral fractions correspond to $z=8.0, 8.75, 9.5$ and $z=7.75, 8.0, 8.25$ as obtained by the Instantaneous and Time-integrated models respectively. This is computed as follows: $\Delta_{\text{xx}}^2 \equiv k^3 / (2\pi^2 V) < |x_{\text{HII}}|^2 > / x_{\text{HI}}^2$ (Hassan et al. 2016).

The Time-integrated model produces more power on large scales by 1-1.2 order of magnitude and less power on small scales by a factor of 2-3, at fixed ionization fraction, as compared to the Instantaneous model. This is consistent with the qualitative impression from the ionisation maps in Figure 3. We further see that the large scale ionization power spectrum, obtained by the Time-integrated EoR model, peaks at $\sim 75 \text{ Mpc}$ which corresponds to the characteristic size of the H II bubbles as seen in the H II maps in figure 3.

The difference particularly on large scales is substantial, which shows the importance of accounting for the existing neutral hydrogen content in the ionization condition (i.e. the second term of equation (5)). Since the fluctuations in the ionisation field drive the 21cm brightness temperature, we expect to see similar differences in the 21cm power spectra, which we examine next.

3.3 The 21cm power spectrum

Using the ionization fields of these models, we now compute our EoR key observable which is the 21cm power spectrum. Assuming that the spin temperature is much higher than the CMB temperature, the 21cm brightness temperature takes the following form:

$$\delta T_b(\nu) = 23 x_{\text{HI}} \Delta \left(\frac{\Omega_b h^2}{0.02} \right) \sqrt{\frac{1+z}{10} \frac{0.15}{\Omega_m h^2}} \left(\frac{H}{H + dv/dr} \right) \text{mK}, \quad (6)$$

where dv/dr is the comoving gradient of the line of sight component of the comoving velocity. Using this equation, it is straightforward to create the 21cm brightness temperature boxes from which we compute the 21cm power spectrum as follows: $\Delta_{21}^2 \equiv k^3 / (2\pi^2 V) < |\delta T_b(\mathbf{k})|^2 >_k$.

Figure 5 shows the 21cm power spectrum of the Instantaneous and Time-integrated models at neutral fractions of 25%, 50% and 75%. Mimicking the ionization field power spectrum, the Time-integrated model produces more power on large scales by 1-1.2 order of magnitude at fixed ionization fraction, as to that of the Instantaneous model. Likewise, the Time-integrated model also produces slightly more power on small scales by a factor of 1.2-1.5 as compared with the Instantaneous EoR model. This difference is less than when comparing the ionization field power spectra, which comes from the contribution of the density field to the 21cm power spectrum – small regions with high local density (high recombinations) remain neutral, and hence they do not contribute much to the small-scale fluctuations in 21cm power.

We also compare our 21cm power spectra to a similar semi-numerical model by Kulkarni et al. (2016) that

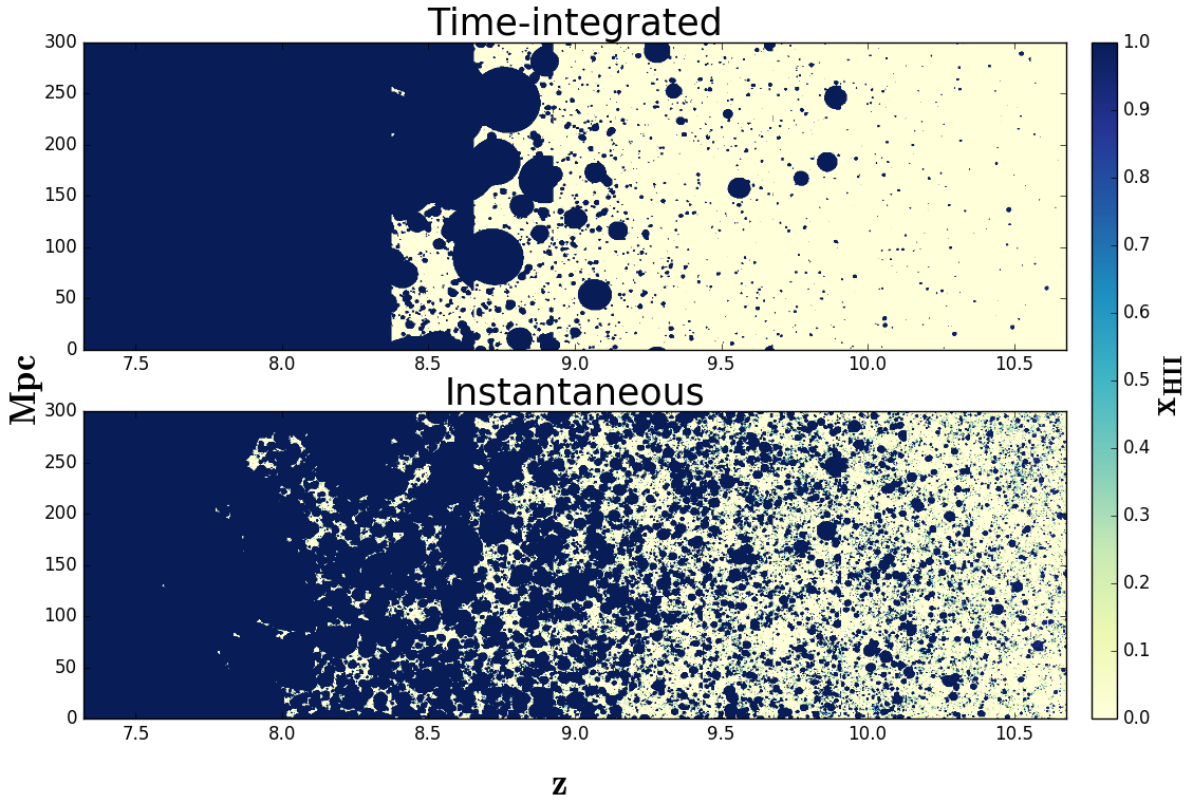


Figure 2. Evolving maps of the neutral fraction from the Instantaneous and Time-integrated models. Time-integrated EoR model produces large HII bubbles and reionizes the universe very rapidly, indicating a sudden EoR scenario. Instantaneous EoR model yields small HII bubbles and reionizes the universe very late, leading to an extended EoR scenario.

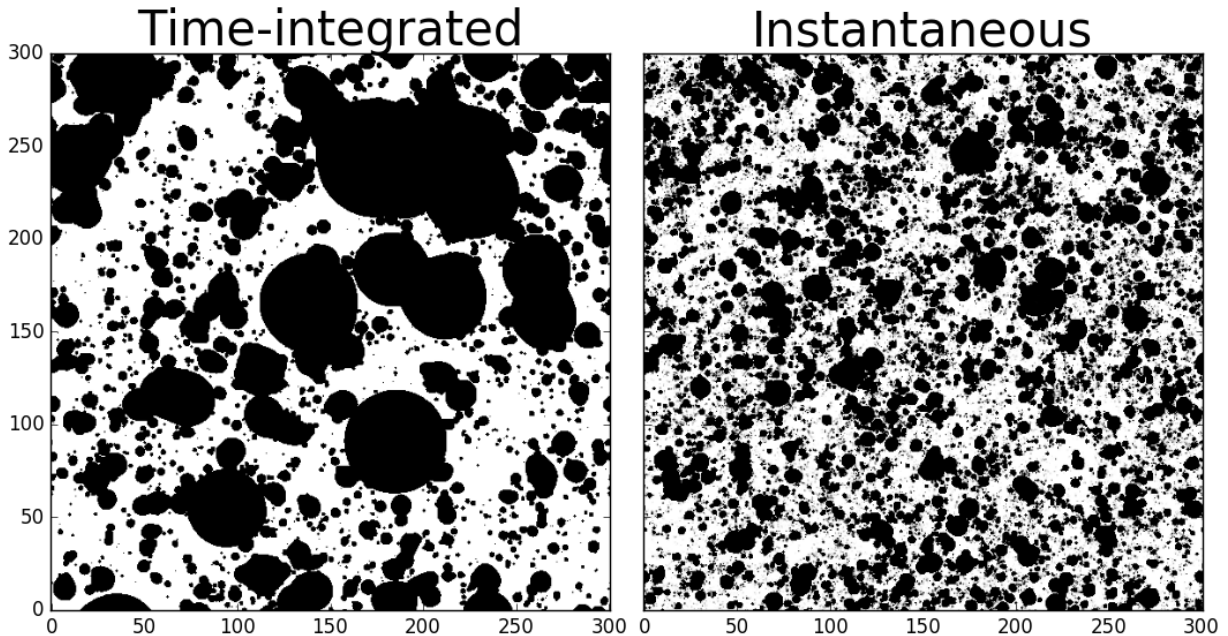


Figure 3. Slice of the ionization box of a size $300 \times 300 \times 0.535 \text{ Mpc}^3$ from the Instantaneous and Time-integrated models and at $x_{\text{HII}} \sim 0.5$. White and black represent neutral and ionized regions respectively.

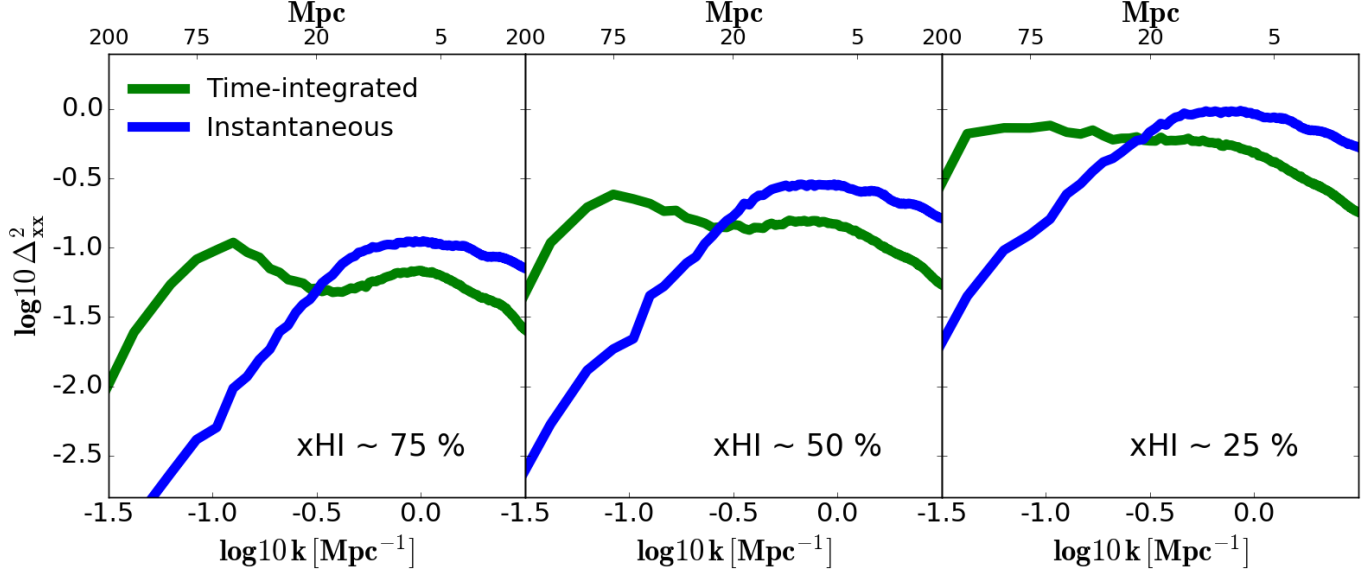


Figure 4. Ionization field power spectrum comparison between the Instantaneous (blue) and Time-integrated (green) models at different stages of reionization ($x_{\text{HI}} \sim 25\%, 50\%, 75\%$.)

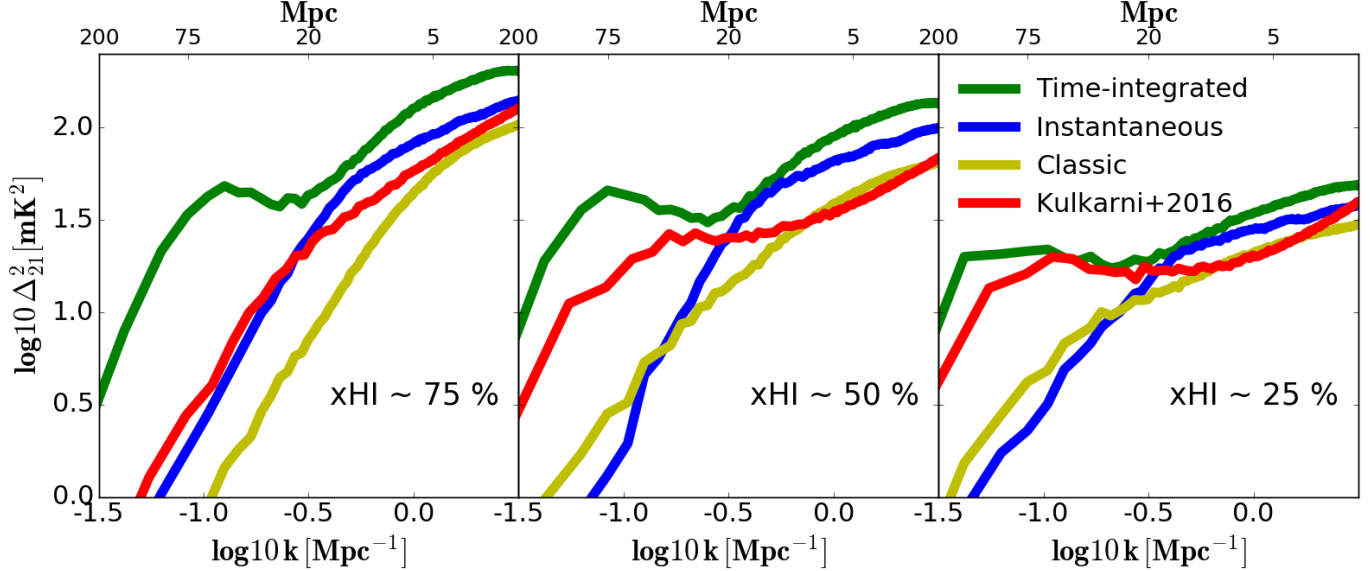


Figure 5. The 21cm power spectrum comparison between the Instantaneous (blue) and Time-integrated (green) models at different stages of reionization ($x_{\text{HI}} \sim 25\%, 50\%, 75\%$). We compare our 21cm power spectra with the Very Late model (red) (tuned to $\tau = 0.055$) by similar semi-numerical method Kulkarni et al. (2016) that is calibrated to match Ly α and CMB data. Although our Time-integrated and Kulkarni et al. (2016) models correspond to different redshifts, but nevertheless the shape of the 21cm spectrum is similar, particularly at the intermediate and late stages of reionizations. We also show our Classic EoR model (yellow) from Hassan et al. (2016) which adopts the standard efficiency parameter approach similar to Kulkarni et al. (2016) model. Our Classic and Kulkarni et al. (2016) models produce similar power on small scales.

has been calibrated with Ly α and CMB data. The semi-numerical models by Kulkarni et al. (2016) adopts the standard efficiency parameter (ζ) approach similar to our Classic EoR model (yellow in fig 5) from Hassan et al. (2016). We choose to compare with the Very Late model in Kulkarni et al. (2016) (red in fig 5) that is tuned to match the Planck (2016) optical depth, consistent with the optical

depth produced by our Time-integrated model. The ionization histories of Kulkarni et al. (2016) and our Time-integrated model are very different even though they obtain $\sim 50\%$ neutral fraction at the same redshift. For instance, our Time-integrated model produces $x_{\text{HI}} = 0.77, 0.57, 0.25$ at $z=8.25, 8.0, 7.75$ whereas Kulkarni et al. (2016) model finds $x_{\text{HI}} = 0.84, 0.59, 0.42$ at $z=10.0, 8.0, 7.0$. Regardless of this

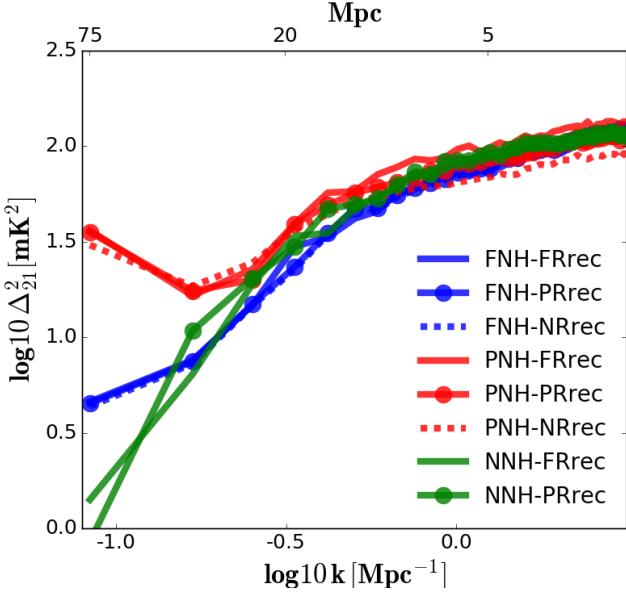


Figure 6. The 21cm power spectrum comparison for different physical assumptions at $x_{\text{HI}} \sim 50\%$. Different colors represent different ways to treat the local fluctuations in the neutral hydrogen density while different line styles corresponds to different recombinations terms, as explained by the legend and text. It is evident that the recombinations are subdominant in determining the large scale 21cm power spectrum. It is also shown models (red), that track the neutral fraction from partially ionized regions, yield a very high 21cm power spectrum on large scales.

difference in these models' reionization histories, their 21cm power spectra are generally similar. We find that both models produce a similar shape of the 21cm power spectrum particularly during the intermediate and final stages of reionization. The minor difference in their amplitudes is due to using our $R_{\text{ion}}-R_{\text{rec}}$ versus the standard ζ approach. This can be clearly seen when comparing our Classic EoR model with Kulkarni et al. (2016) model in figure 5. We see both models produce the same power on small scales while their difference on large scales might be from the difference in the density field and neutral fractions. This confirms our previous findings that using the non-linear ionization power, via our $R_{\text{ion}}-R_{\text{rec}}$ approach, boosts the 21cm power spectrum as compared to models adopting the standard efficiency parameter method (Classic and Kulkarni et al. (2016) models).

This shows that our Time-integrated model, that is calibrated to match various EoR key observables, produces similar 21cm power spectrum as obtained by other semi-numerical models that have been calibrated to match $\text{Ly}\alpha$ and CMB data. The future 21cm observations might be able to discriminate between these models' power spectra.

In summary, we have compared the Instantaneous and Time-integrated models in terms of their EoR history, topology, and their 21cm power spectra. We have found that the Time-integrated model produces large HI bubbles while the Instantaneous model produces more small HI bubbles. The Time-integrated model yields a large scale 21cm/Ionization power spectrum that is higher by 1 order of magnitude as compared with the Instantaneous model. We have seen that the ionization condition (equation (5)) results in large HI bubbles which boost the amount of power on large scales.

4 MODEL ASSUMPTION EFFECTS ON THE 21CM POWER SPECTRUM

The large differences in the 21cm power spectrum (figure 5) between the Instantaneous and Time-integrated models show that the 21cm power spectrum is highly sensitive to the physical assumptions used. There are two main differences between these models: First, the ionisation condition now accounts for the number of hydrogen atoms, and second, the recombination is now done accounting for partial ionisation. We believe our new model is more physically-motivated and realistic, but we would like to understand exactly how these changes individually impact the 21cm power spectra.

We therefore consider the various possible combinations between R_{rec} and N_{H} to create several models with different ionization condition. We also consider models neglecting recombination altogether to analyse the impact of recombinations as we did in Hassan et al. (2016), only with our new Time-integrated model.

More specifically, we keep the LHS of equation (5) (R_{ion} term) same and vary the RHS terms to create the following models:

- Full-NH-Full-Rrec (**FNH-FRrec**): $R_{\text{rec},V} + N_{\text{H}}$.
- Full-NH-Partial-Rrec (**FNH-PRrec**): $x_{\text{HI}} R_{\text{rec},V} + N_{\text{H}}$.
- Full-NH-No-Rrec (**FNH-NRrec**): N_{H} .
- Partial-NH-Full-Rrec (**PNH-FRrec**): $R_{\text{rec},V} + (1 - x_{\text{HI}}) N_{\text{H}}$.
- Partial-NH-Partial-Rrec (**PNH-PRrec**): $x_{\text{HI}} R_{\text{rec},V} + (1 - x_{\text{HI}}) N_{\text{H}}$.
- Partial-NH-No-Rrec (**PNH-NRrec**): $(1 - x_{\text{HI}}) N_{\text{H}}$.
- No-NH-Full-Rrec (**NNH-FRrec**): $R_{\text{rec},V}$.
- No-NH-Partial-Rrec (**NNH-PRrec**): $x_{\text{HI}} R_{\text{rec},V}$.

The Time-integrated model is represented here by ionization condition of **PNH-PRrec** whereas the Instantaneous model uses that of **NNH-FRrec**. The others are variants on these. To illustrate the differences in the 21cm power spectrum, we use the same density field and halo catalogues generated within a simulation run of a box size 75 Mpc and $N = 140^3$. We have shown previously (Figure 8 in Hassan et al. 2016) that the numerical volume convergence of our simulated 21cm power spectrum is excellent at all redshifts down to a box size of 75 Mpc, hence, we expect the same 21cm power spectrum for larger simulation volumes. The reionisation history produced by these models vary, so as before we choose to make our 21cm power spectrum comparison at a fixed neutral fraction.

Figure 6 shows the 21cm power spectrum produced by different models at 50% neutral fraction as explained above. First, we see that all these variants result in virtually the same 21cm power spectrum on small scales. This reiterates our previous finding in Hassan et al. (2016) that using a non-linear ionisation rate R_{ion} boosts the 21cm power spectrum by a similar amount regardless of whether one accounts for recombinations or not, and further shows that accounting for the neutral hydrogen atoms does not alter this conclusion.

More significant differences are evident at large scales for the 21cm power spectrum. Models starting with full N_{H} (**FNH-**) produce 21cm power spectra with the same shape and amplitude on all scales (i.e. all the blue lines overlap), and likewise for models with partial or no N_{H} (**PNH-** and **NNH-**). This demonstrates that recombinations are sub-

dominant for determining the large-scale 21cm power spectrum. It is clear that the **NH** term plays a major role in boosting/suppressing the large scale 21cm power spectrum. This means that semi-numerical models must carefully account for the local number density of neutral hydrogen for a proper prediction of the expected signal.

From figure 6, we see the clear trend that models that do not account for the existing neutral hydrogen atoms (**NNH**-models such as the Instantaneous model) have lower 21cm power spectrum on large scales. Furthermore, models that use the total number of hydrogen atoms (**FNH**- models) at each time-step regardless of the ionization fraction show 21cm power spectra that is slightly higher on large scales as compared to **NNH**- models. This is due to the presence of weak HI fluctuations by following only the density field ($\mathbf{N}_{\text{HI}} \sim \Delta$). However, models, that use the ionization history of cells to track the neutral hydrogen atoms from partially ionised regions (**PNH**- models such as the Time-integrated model), show a very high 21cm power spectrum on large scales as opposed to the **NNH**- and **FNH**- models. This comes from the fact that the **PNH**- models account for a strong HI fluctuations by following the density field ($\mathbf{N}_{\text{HI}} \sim \Delta$) and ionization field ($\mathbf{N}_{\text{HI}} \sim \mathbf{x}_{\text{HII}}$) both. This shows that, at given neutral fraction, the large scale 21cm power spectrum is highly influenced by the way in which we account for the fluctuations in the local neutral hydrogen density.

In the next section, we will discuss the calibration of the Time-integrated model against various EoR key observables and test how well the ongoing/upcoming 21cm observations will further constraints our free parameters.

5 MODEL CALIBRATION

We now focus on our favoured Time-integrated reionisation model, which includes all our new physics implementations. Previously, the parametrization of R_{ion} (equation (2)) was obtained from our small-volume high-resolution radiative transfer hydrodynamic simulation (6/256-RT). However, the small volume of this simulation makes it subject to uncertainties since, as we saw in Figure 1, the ionisation history of this simulation is significantly delayed by its small volume. Here, we adopt a more general form for R_{ion} , and determine whether existing EoR measurements can calibrate our source model, and thereby provide constraints on the nature of reionising sources.

To this end, we here consider a more generalized model with the following three free parameters:

- f_{esc} is the volume-averaged photon escape fraction.
- A_{ion} is the ionising emissivity amplitude, which scales the amount of ionising emissivity (R_{ion}) equally across the halo mass range at a given redshift.
- C_{ion} is ionising emissivity-halo mass power dependence, which quantifies the $R_{\text{ion}}-M_h$ slope.

We will constrain these three parameters against various EoR observations and compare with the values found from fitting to the 6/256-RT simulation, using a Bayesian MCMC approach.

Recall that the Time-integrated model identifies the ionised regions using a time dependent ionization condition

(equation (5)), that tracks the exact recombinations and neutral hydrogen atoms by following the reionization history. The reionization history, in this model, is numerically well converged for $\Delta z \leq 0.125$. With these requirements, the model becomes more computationally expensive to run, but nevertheless, is feasible for independent large volume runs. However, sampling the full MCMC space requires at least $\sim 10^6$ simulation realizations, which becomes infeasible. Hence we precompute a grid of models spanning the full prior space, and then do a trilinear interpolation to obtain the observables for any given parameter combination. This sacrifices some accuracy but makes the computation feasible.

We note that Greig & Mesinger (2015) developed an analysis pipeline, 21CMMC, that directly links their semi-numerical model 21CMFAST (Mesinger et al. 2011) to a Bayesian routine COSMOHAMMAR (Akeret et al. 2013) to constraining their free parameters. However, their ionisation condition did not include recombinations through the time integral method which they developed in Sobacchi & Mesinger (2014), and instead used a standard efficiency parameter (ζ) approach. Along with lower resolution of ~ 2 Mpc, these simplifications enabled them to run their semi-numerical model fully within an MCMC scheme.

5.1 Parameter estimations pipeline

We choose a cell size of $0.375 \text{ h}^{-1} \text{ Mpc}$ and a box size $L = 75 \text{ Mpc}$, giving $N = 140$ cells per side. We precompute a grid of $25 \times 25 \times 25$ runs outputting the predicted observables for our models, uniformly sampling our selected prior range for our parameters of ($f_{\text{esc}}, \log_{10}(A_{\text{ion}}), C_{\text{ion}}$) = $[(0,1),(37,44),(-1,2)]$. This gives a total of 15,625 simulation independent realizations, which we interpolate inside the MCMC search process.

We have tested our parameter constraints using two different Bayesian inference tools MULTINEST (Feroz et al. 2009) and EMCEE (Foreman-Mackey et al. 2013). We have found the same parameter estimates using these two different codes, and hence, our presented parameters estimation here appear to be robust to variations in the algorithm used.

We here present the results obtained by using the EMCEE python package. We use 100 random walkers initialised around the maximum likelihood. For each walker, we sample 10,000 chains from the likelihood after 500 initial burn-in chains to achieve convergence. This makes a total of 1,000,000 samples which is sufficient to explore the whole parameter space.

5.2 EoR key observables constraints

We constrain our three free parameters to the following observations:

- The dust-corrected star formation rate density integrated down to $M_{\text{AB}} = -17$ by Bouwens et al. (2015) at the following redshifts:

- $z \sim 6$: $\log_{10}(\text{SFR}) [\text{M}_{\odot} \text{ Mpc}^{-3} \text{ yr}^{-1}] = -1.55 \pm 0.06$.
- $z \sim 7$: $\log_{10}(\text{SFR}) [\text{M}_{\odot} \text{ Mpc}^{-3} \text{ yr}^{-1}] = -1.69 \pm 0.06$.
- $z \sim 8$: $\log_{10}(\text{SFR}) [\text{M}_{\odot} \text{ Mpc}^{-3} \text{ yr}^{-1}] = -2.08 \pm 0.07$.

- The Planck (2016) integrated optical depth to Thomson scattering: $\tau = 0.058 \pm 0.012$.

EoR Constraint	f_{esc}	$\log_{10}(A_{\text{ion}})$	C_{ion}
Bouwens et al. (2015) SFR all at $z=6,7,8$	$0.51^{+0.33}_{-0.34}$	$39.61^{+0.18}_{-0.16}$	$0.45^{+0.08}_{-0.09}$
Planck (2016) optical depth τ	$0.46^{+0.36}_{-0.32}$	$39.08^{+1.39}_{-1.44}$	$0.28^{+0.76}_{-0.88}$
Becker & Bolton (2013) ionizing emissivity N_{ion} at $z=4.75$	$0.51^{+0.34}_{-0.34}$	$39.68^{+0.93}_{-1.36}$	$-0.12^{+0.78}_{-0.62}$
ALL = SFR + τ + N_{ion}	$0.25^{+0.26}_{-0.13}$	$39.62^{+0.17}_{-0.18}$	$0.44^{+0.09}_{-0.09}$
Values obtained from fitting to 6/256-RT	-	40.03	0.41

Table 1. Summary of our parameter estimations from individual and combined set of observations, as well as from matching to the 6/256-RT simulations.

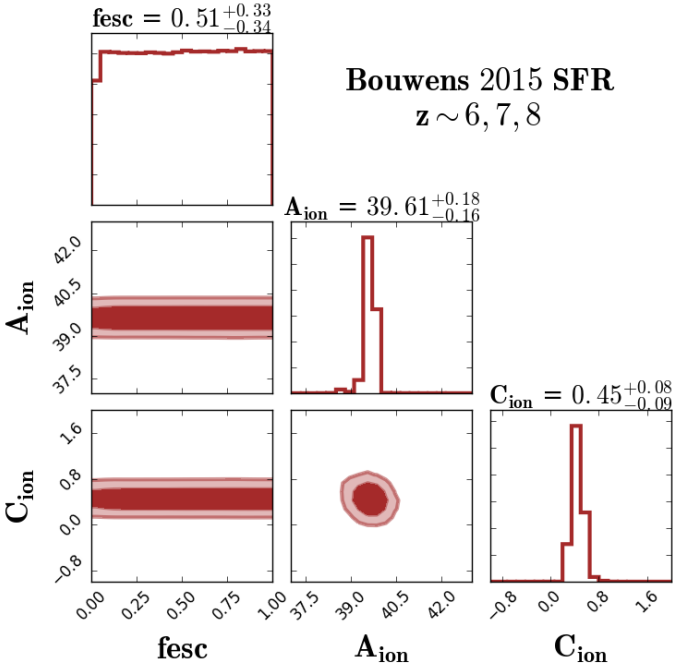


Figure 7. Bouwens et al. (2015) SFR observations, at $z=6,7,8$ combined together, constraints on our model parameters. Values on top of the 1-D PDFs diagonal represent the best fit parameters with $1-\sigma$ (14th and 84th percentiles). Dark and light shaded regions correspond to $1-\sigma$ and $2-\sigma$ levels respectively. The Bouwens et al. (2015) SFR observations provide tight constraints on the A_{ion} and C_{ion} in the selected prior range. As expected, the SFR measurements don't constrain the f_{esc} .

(iii) The Becker & Bolton (2013) ionising emissivity density measurements from Ly α data at $z = 4.75$: $\dot{N}_{\text{ion}} [10^{51} \text{ photons s}^{-1} \text{ Mpc}^{-3}] = -0.014^{+0.454}_{-0.355}$.

We will first examine how our free parameters are constrained individually by each observation, and then we will examine the combined constraints.

5.2.1 The Bouwens et al. (2015) SFR constraints

Unlike other semi-numerical models that rely on the efficiency parameter ζ , our model allows a direct comparison to the SFR measurements by using a parameterisation for R_{ion} that is directly relatable to SFR. For a consistent compar-

ison with Bouwens et al. (2015) measurements, we convert the R_{ion} back to SFR using Equation (2) in Finlator et al. (2011) that is based on Schaerer (2003) models, and add up all SFR from halos brighter than $M_{\text{AB}} = -17$ at $z = 6, 7, 8$.

Figure 7 shows the posterior distribution of our parameters as constrained solely by Bouwens et al. (2015) integrated SFR observations at $z=6,7,8$ (taken together). This provides somewhat tighter constraints than fitting to a single redshift of SFR measurement, although constraining to a single redshift yields similar results, which indicates that the weak redshift evolution in the SFR measurements is adequately reproduced by our model for R_{ion} .

The Bouwens et al. (2015) SFR observations provides tight constraints on the A_{ion} and C_{ion} as seen in figure 7. while poorly constraining f_{esc} . The latter is expected because the f_{esc} is set by the recombinations in the ISM while the SFR depends on the halo mass and redshift.

The value of $C_{\text{ion}} = 0.45$ agrees within the $1-\sigma$ level with what was previously found from fitting our hydrodynamical simulations, which yielded $C_{\text{ion}} = 0.41$ (Hassan et al. 2016). This means that our large volume semi-numerical model is compatible with the same slope of the $R_{\text{ion}}-M_h$ relation predicted by the small volume 6/256-RT simulation to match the Bouwens et al. (2015) SFR observation, thereby nicely corroborating the direct simulation results.

However, the differences are more significant in the A_{ion} posterior distribution. We see that the A_{ion} best-fit value of $10^{40.03}$ predicted by 6/256-RT simulation over-estimates by $\sim 50\%$ the value of $A_{\text{ion}} = 10^{39.61}$ favoured by our SIMFAST21 MCMC fit using only the Bouwens et al. (2015) SFR constraints. This represents somewhat poor concordance at only a $3-\sigma$ level. This discrepancy arises due to the small box size ($=6h^{-1}\text{Mpc}$) of 6/256-RT simulation that does not capture the large scale fluctuations and massive dark matter halos that contribute significantly to the reionisation photon budget. Hence, the 6/256-RT simulation requires larger A_{ion} to compensate for these limitations. This effect is also seen in figure 1 when comparing the reionization histories of the 6/256-RT simulation with our large volume semi-numerical simulations which tend to reionize the universe much earlier at a fixed optical depth due to the presence of those massive halos and large scale-fluctuations.

Overall, utilising only the integrated SFR observations already gives interesting constraints on the slope and amplitude of the ionising photon output as a function of halo mass. However, there are no useful constraints on the escape fraction.

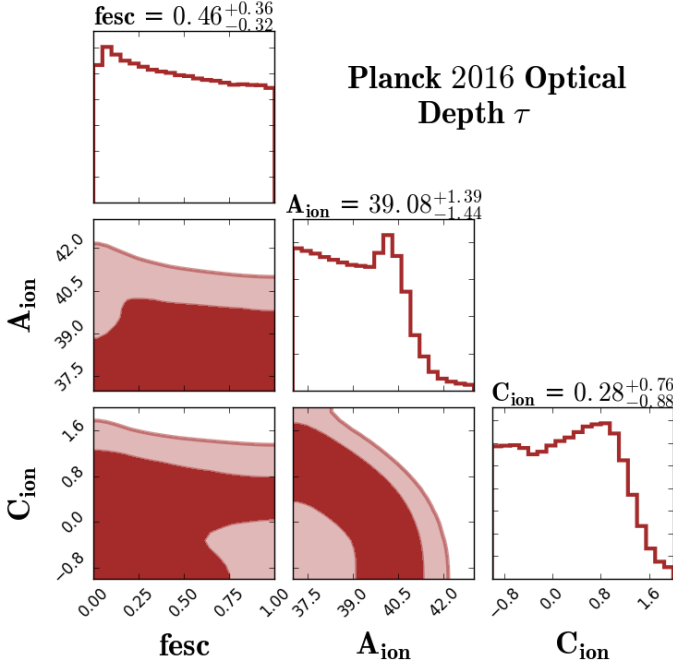


Figure 8. Planck (2016) optical depth constraints on our model parameters. Values on top of the 1-D PDFs diagonal represent the best fit parameters with $1\text{-}\sigma$ (14th and 84th percentiles). Dark and light shaded regions correspond to $1\text{-}\sigma$ and $2\text{-}\sigma$ levels respectively. The Planck (2016) τ provides poor constraints on all parameters while there is slight tendency towards lower f_{esc} values. The Planck (2016) τ prefers models with low A_{ion} and C_{ion} values for the chosen prior range as compared to values implied by the Bouwens et al. (2015) SFR observations.

5.2.2 The Planck (2016) optical depth constraints

Figure 8 shows the parameters constrained to match solely the Planck (2016) data. This shows that the Thomson optical depth data alone provides fairly poor constraints on any of the parameters. There is a slight tendency to favour lower f_{esc} values, as also found by Greig & Mesinger (2016, see their Figure 4), but in general all values from zero to one are still allowed.

The main reason for the lack of sensitivity to f_{esc} is shown in Figure 9, and essentially arises from the still-large errors on τ . Figure 9 shows the volume-weighted global neutral fraction evolution for fixed values of A_{ion} and C_{ion} , and shows that $f_{\text{esc}} = 20 \rightarrow 80\%$ gives rise to $\tau = 0.058 \rightarrow 0.071$, which is still essentially within the 1σ uncertainty on the measurement of $\tau = 0.058 \pm 0.012$. Hence much smaller error bars on τ are required to provide better constraints on f_{esc} .

A_{ion} and C_{ion} are also not well constrained by the Thomson optical depth data alone, though there is some tendency to favour small values of A_{ion} and C_{ion} . Nonetheless, the uncertainties are large, and the values favoured from the SFR constraints alone are within the 1σ uncertainties of these predictions, as are the values found directly from the hydrodynamic simulations.

In summary, the Thomson optical depth as measured by Planck alone does not provide strong constraints on any of our parameters. It is clear that reducing uncertainties

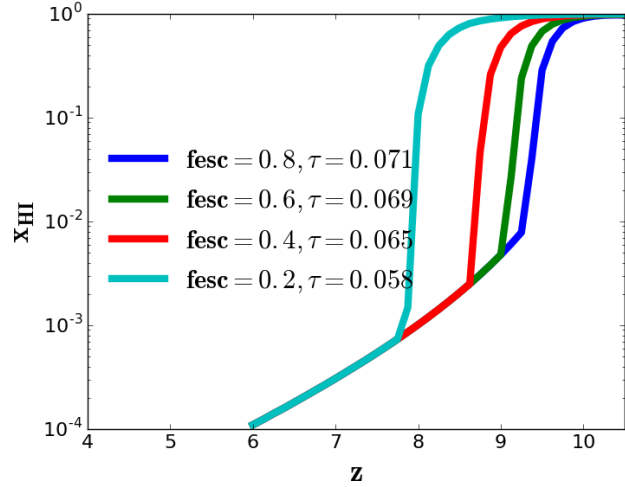


Figure 9. The reionization history for our Time-integrated model with different f_{esc} values while fixing the A_{ion} and C_{ion} to values implied by the recent Planck (2016) τ measurements. This clearly shows that the current Planck (2016) optical depth $\tau = 0.058 \pm 0.012$ does not provide tight f_{esc} constraints for models with rapid reionization scenarios as the case with our Time-integrated EoR model.

and/or including other data will be required in order to meaningfully constrain the sources driving reionisation.

5.2.3 The Becker & Bolton (2013) ionizing emissivity constraints

The integrated emissivity of ionizing photons \dot{N}_{ion} quantifies the total ionization rate density from all ionizing sources that escape galaxies to fill the intergalactic medium. To compare with Becker & Bolton (2013) \dot{N}_{ion} measurements, we add up $f_{\text{esc}} R_{\text{ion}}$ from all halos and divide by the simulation comoving volume at $z=4.75$. As with the SFR data, our model permits a direct comparison with the \dot{N}_{ion} data since we use a parameterisation for R_{ion} rather than a single efficiency parameter.

Figure 10 shows the posteriors for our three free parameters constrained only to match the Becker & Bolton (2013) \dot{N}_{ion} data. As with the SFR and τ constraints, the f_{esc} is unconstrained by this data. Similar to Planck (2016) τ constraints, we find that models with high A_{ion} and C_{ion} values are disfavored by Becker & Bolton (2013) \dot{N}_{ion} measurements, but again this is within 1σ of the SFR-only constraints.

The slight tendency of \dot{N}_{ion} data towards negative values of C_{ion} (negative slope of $R_{\text{ion}}\text{-}M_h$ relation) favours small halos being the dominant ionizing photon sources contributor to match the post-reionization measurements. In contrast, SFR and τ data prefers the positive side of C_{ion} values, implying that massive halos are more important during the reionization. This shows that reionization requires more ionising photons while matching post-reionization data requires fewer ionising photons. This stands as one of the theoretical challenges for the EoR models as it is not easy to match simultaneously observational constraints during and after reionizations. \dot{N}_{ion} measurements at higher redshifts

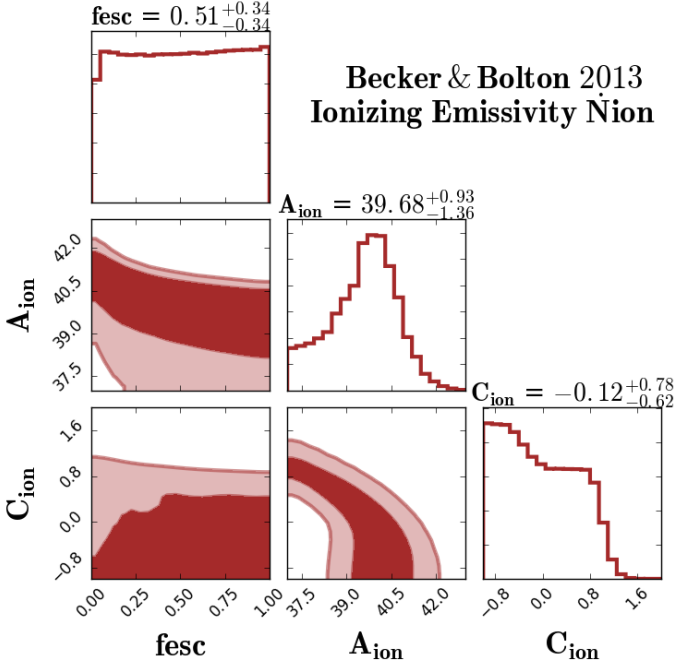


Figure 10. The Becker & Bolton (2013) ionizing emissivity ($z=4.75$) constraints on our model parameters. Values on top of the 1-D PDFs diagonal represent the best fit parameters with $1\text{-}\sigma$ (14th and 84th percentiles). Dark and light shaded regions correspond to $1\text{-}\sigma$ and $2\text{-}\sigma$ levels respectively. Similar to previous constraints, the f_{esc} is poorly constrained and similar to τ constraints, the data prefers lower f_{esc} values. The Nion data also prefers models with negative C_{ion} in our selected prior range. This shows that matching to post-reionization data requires fewer ionising photons and prefers models with dominant contributions from small dark matter halos.

($z \sim 6, 7$) would be very useful to see if this tension extends into the overlapping redshift regime (Keating et al. 2014).

5.2.4 Combined SFR + τ + Nion constraints

To obtain the strongest constraints given the observations we consider, we now combine our three key EoR constraints: the Bouwens et al. (2015) SFR observations, Planck (2016) optical depth measurements and the Becker & Bolton (2013) Nion data. This represents the best available constraints we can make given current data, and serves to provide our base model from which we will do forecasting for 21cm experiments.

Figure 11 shows the parameter estimates as fit to the combined sample of these EoR observations. We see that the A_{ion} and C_{ion} are tightly constrained, which as Figure 7 showed is driven by the Bouwens et al. (2015) SFR constraints, as the other observations did not provide very tight constraints on these parameters.

The more interesting difference is in f_{esc} , where the combined constraints now definitely prefers lower f_{esc} values, with best-fit-value of $0.25^{+0.26}_{-0.13}$. This is still a rather wide range, and the posterior ellipses show that even very low escape fractions are not ruled out at more than a $\sim 1\sigma$ level, and very high f_{esc} values are only disfavoured at $\lesssim 2\sigma$. This tendency was hinted at from matching to Becker &

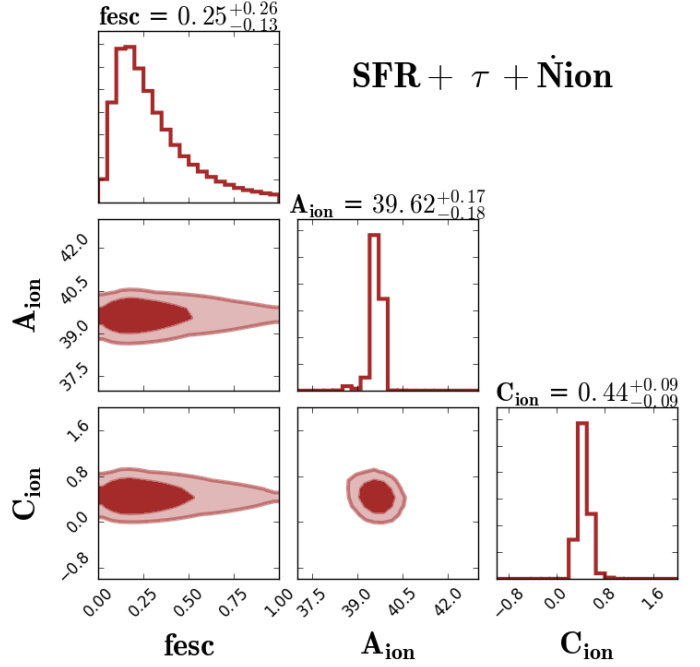


Figure 11. Combined constraints from SFR, τ and Nion. Values on top of the 1-D PDFs diagonal represent the best fit parameters with $1\text{-}\sigma$ (14th and 84th percentiles). Dark and light shaded regions correspond to $1\text{-}\sigma$ and $2\text{-}\sigma$ levels respectively. Combining all these observations results in a tighter f_{esc} constraints while A_{ion} and C_{ion} still follow Bouwens et al. (2015) SFR constraints.

Bolton (2013) Nion and Planck (2016) optical depth individually. This result indicates that our previous findings of $f_{\text{esc}} = 0.04 - 0.06$ in Hassan et al. (2016) is clearly possible for models with higher A_{ion} and C_{ion} values within their derived $1\text{-}\sigma$ level. A summary of the individual and combined constraints is provided in Table 1.

This shows that current observations can already constrain the basic power law parameters of the ionising photon output versus halo mass, but constraints on f_{esc} are still somewhat elusive. Note that we are also assuming a constant f_{esc} for all galaxies, while there may be some mass and/or redshift dependence; however, with even a single parameter already being poorly constrained, it is unlikely that adding more parameters will allow tighter constraints.

6 21CM FORECASTING AND EXPERIMENTS SENSITIVITIES

The ultimate goal is to add the 21cm observations to these existing data (or future improved versions thereof), in order to ascertain how well we can understand the sources of reionisation. To do so, we adopt a forecasting approach by which we use expected uncertainties from future 21cm power spectrum measurements in concert with these existing data and ascertain how much improvement the 21cm data will provide in the precision with which our parameters are constrained. We will assume a base model that is the best-fit to our current constraints as listed in Table 1.

We focus our analysis on LOFAR, HERA, and SKA1-

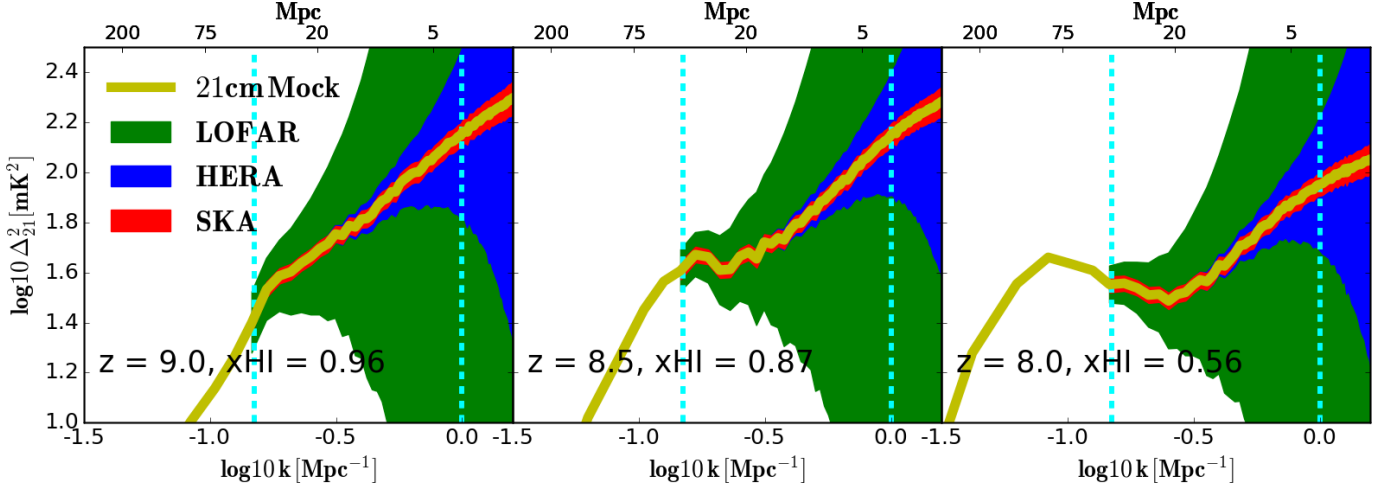


Figure 12. Three redshifts mock 21cm EoR observations using the well-calibrated Time-integrated EoR model with parameters $(f_{\text{esc}}, \log_{10}(A_{\text{ion}}), C_{\text{ion}}) = (0.24, 39.63, 0.43)$. Yellow solid line represents the 21cm power spectrum from the Large box mock observation ($L=300/N=560$). Shaded area shows the errorbars obtained using 21CMSENSE package for our constructed EoR arrays: SKA (red), HERA (blue), LOFAR (green). Redshifts and neutral fractions for 21cm mock observations are quoted in each panel. Vertical cyan dashed lines show our chosen k -range to preform the 21cm MCMC.

Low. For each experiment, we first compute the thermal noise power spectrum which dominates the errors in measuring the 21cm signal. We then add more uncertainties from the sample variance, while neglecting the shot noise since it has been shown to have a minimal effect at the relevant scales ($k < 2h\text{Mpc}^{-1}$) for these telescopes sensitivities (Pober et al. 2013). We obtain these uncertainties using the 21CMSENSE package⁴, and refer to Parsons et al. (2012) for the full mathematical derivation of the radio interferometer sensitivities, and to Pober et al. (2013, 2014) for more details on observation strategies and foreground removal models. We briefly highlight the basic equations and concepts used in 21CMSENSE to obtain the 21cm power spectrum error from a specific array configuration.

The dimensionless power spectrum of the thermal noise (Parsons et al. 2012; Pober et al. 2013, 2014) can be obtained using:

$$\Delta_N^2(k) \approx X^2 Y \frac{k^3}{2\pi^2} \frac{\Omega}{2t} T_{\text{sys}}^2, \quad (7)$$

where $X^2 Y$ is a conversion factor from angle and frequency units to comoving cosmological distances, Ω is the primary beam field-of-view, t is the integration time and T_{sys} is the system temperature (sky+receiver). It is then straightforward to add the sample variance to the thermal noise to obtain the total error (Pober et al. 2013) as follows:

$$\delta\Delta^2(k) = \left(\sum \frac{1}{(\Delta_N^2(k) + \Delta_{21}^2(k))^2} \right)^{-\frac{1}{2}}, \quad (8)$$

where Δ_{21}^2 is the 21cm power spectrum and the summation runs over all measured independent k -modes.

We construct these experiments as follows:

- **LOFAR:** We use the Netherlands 48 High-Band An-

tennas (HBA) with positions listed in van Haarlem et al. (2013) following Pober et al. (2014). Each antenna has a diameter of 30.75 m which results in a total collecting area of 35,762 m² for the 48 HBA station. The receiver temperature T_{rcvr} is set to 140,000 mK as suggested by Jensen et al. (2013); Greig & Mesinger (2015).

- **HERA:** We consider the final design of 331 hexagonally packed 14 m antennas (Ewall-Wice et al. 2016; Beardsley et al. 2015). With this configuration, the total collecting area becomes 50,953 m². We assume an 100,000 mK receiver temperature T_{rcvr} , similar to previous works by Pober et al. (2014); Greig & Mesinger (2015).

- **SKA-LOW1:** We model SKA1-Low following the SKA1 System Baseline Design document by Dewdney (2013) in which the proposed array consists of 911 antennae in total. These antennae are distributed randomly to form a compact core using 866 dishes surrounded by the remaining 45 dishes along spiral arms. The 866 core antennae provide the vast majority of the sensitivity, and hence our SKA model ignores those 45 spiral arms stations (Pober et al. 2014; Greig & Mesinger 2015). Each station of 866 antennae has a diameter of 35 m which makes a total collecting area of 833,189 m². The receiver noise here is determined by: $T_{\text{rcvr}} = 0.1 T_{\text{sky}} + 40$ K, where the sky temperature is modelled using: $T_{\text{sky}} = 60\lambda^{2.55}$.

For a consistent comparison, we choose to operate these three array designs in a drift-scanning mode for 6 observing hours per day for 180 days at 8 MHz bandwidth. We consider Pober et al. (2014) moderate foreground removal model where the foreground wedge extends 0.1 h Mpc⁻¹ beyond horizon limit.

6.1 Including the 21cm data

We combine three different redshifts of 21cm power spectrum observations, namely $z = 9.0, 8.5, 8.0$, which provides

⁴ <https://github.com/jpober/21cmSense>

	f_{esc}	$\log_{10}(A_{\text{ion}})$	C_{ion}
21cm Mock Observations			
SKA	$0.240^{+0.056}_{-0.054}$	$39.628^{+0.030}_{-0.032}$	$0.431^{+0.052}_{-0.056}$
HERA	$0.237^{+0.061}_{-0.054}$	$39.626^{+0.031}_{-0.025}$	$0.425^{+0.055}_{-0.058}$
LOFAR	$0.415^{+0.384}_{-0.239}$	$39.229^{+0.606}_{-1.117}$	$0.445^{+0.341}_{-0.274}$
21cm Mock Observations + ALL (SFR, \dot{N}_{ion}, τ)			
SKA+ALL	$0.217^{+0.052}_{-0.048}$	$39.631^{+0.024}_{-0.029}$	$0.423^{+0.053}_{-0.057}$
HERA+ALL	$0.221^{+0.058}_{-0.051}$	$39.630^{+0.029}_{-0.029}$	$0.427^{+0.053}_{-0.059}$
LOFAR+ALL	$0.206^{+0.069}_{-0.045}$	$39.634^{+0.042}_{-0.033}$	$0.421^{+0.065}_{-0.060}$

Table 2. Summary of our parameter estimations from the 21cm mock observations and from combining the 21cm mock observations with the current EoR observations (SFR, \dot{N}_{ion} , τ).

tighter constraints than considering any single epoch observations. With multiple redshifts 21cm observations, one accounts simultaneously for the variation in redshift (density field) and neutral fraction (ionisation field) evolution, which are the main components in determining the 21cm fluctuations. Given the rapid reionization behaviour of the Time-integrated model as shown in figure 1, our selected redshifts ($z = 9, 8.5, 8$) correspond to a wide range of neutral fractions that account for different reionisation epochs such as the initial bubble growth and the bubble overlap phase. We next construct the likelihood from these observations by simply adding up their individual χ^2 . We limit our analysis to a wide k -range of $0.15\text{--}1.0\text{ Mpc}^{-1}$, consistent with Greig & Mesinger (2015). From this k -range, we select 10 bins of the power spectrum which is sufficient to capture the fluctuations for a given 21cm power spectrum.

We use the well-calibrated Time-integrated model with parameters derived from fitting to our combined set of EoR observations as discussed in § 5.2.4 and shown in figure 11. Specifically, we use the following parameters: $(f_{\text{esc}}, \log_{10}(A_{\text{ion}}), C_{\text{ion}}) = (0.24, 39.63, 0.43)$, consistent with the $1\text{-}\sigma$ level of constraints by our combined set of EoR observations. We then use these parameters to create our mock observations with a large box size of $L = 300\text{ Mpc}$ and $N = 560$ per side which results in a resolution of $0.375\text{ }h^{-1}\text{ Mpc}$. We determine the error in measuring the 21cm power spectra for our mock observation by using the telescope sensitivity code 21CMSENSE for each specific array experiments at our chosen redshifts as described above. We use the same pipeline discussed in § 5.1 to sample the 21cm power spectrum space, except now we include the 21cm mock observation power spectra among the pre-computed runs to study how well the MCMC technique may recover the input model parameters.

Figure 12 shows our 21cm mock observations at several redshifts. The shaded area corresponds to the error in measuring the 21cm power spectrum for our large mock observations using the 21CMSENSE package. LOFAR (green shading), operating currently, will be able to constrain only the largest scales considered here, while HERA (blue), under construction now, will be further sensitive to intermediate scales, while the future SKA1-Low (red) will provide tight

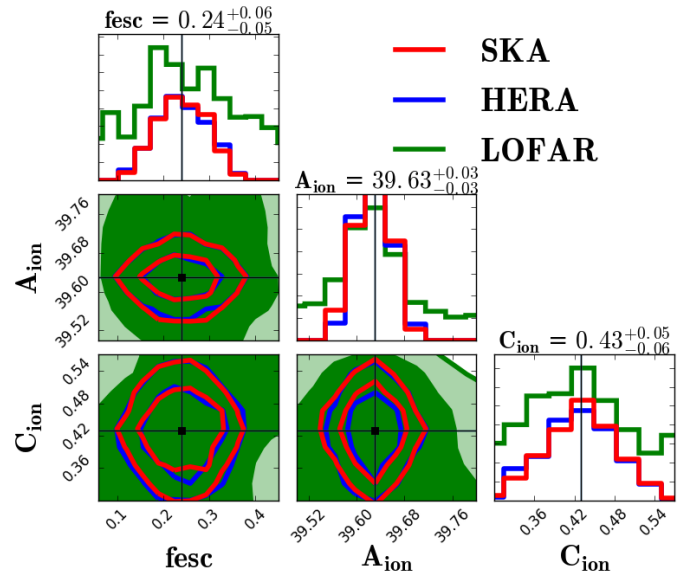


Figure 13. 21cm power spectrum constraints on our three EoR parameters from several redshifts ($z=9.0, 8.5, 8.0$) mock observations. SKA, HERA, and LOFAR constraints are shown by red, blue, and green contours respectively. Values on top of the 1D PDFs represent the best fit parameters as implied by the SKA mock observations while black square points correspond to the input mock observation parameters: $(f_{\text{esc}}, \log_{10}(A_{\text{ion}}), C_{\text{ion}}) = (0.24, 39.63, 0.43)$. The MCMC technique is able to recover the input model parameters. It is evident that the future 21cm observations can tightly constrain our model parameters for experiments with small and intermediate levels of uncertainty in detecting the expected signal such as SKA and HERA respectively.

constraints into the sub-Mpc scale regime owing to its wider baselines and hence better resolution. These uncertainties depend mainly on our telescope configurations as described above. Hence the main improvement as these facilities develop will be to better constrain the 21cm power spectrum towards smaller scales, and each generation will provide significant gains in this.

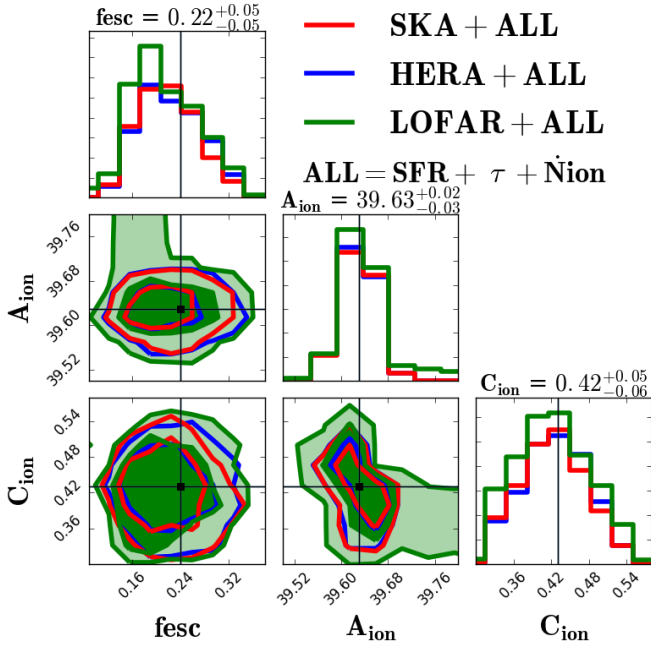


Figure 14. Parameter estimates from combining the current EoR observations with the 21cm mock observations. The current EoR observations here are our previous combined sample: SFR, τ and \dot{N}_{ion} while the 21cm mock observations are combinations of several 21cm redshifts at $z=9.0, 8.5, 8.0$. SKA, HERA, and LOFAR constraints are shown by red, blue, and green contours respectively. Values on top of the 1D PDFs represent the best fit parameters as implied by the SKA mock observations while black square points correspond to the input mock observation parameters: $(f_{\text{esc}}, \log_{10}(A_{\text{ion}}), C_{\text{ion}}) = (0.24, 39.63, 0.43)$. It is evident that adding the current EoR observations on top of the 21cm mock observations provide more tighter constraints even for experiments with large 21cm power uncertainties such as the case with LOFAR.

6.2 21cm MCMC

We now ask how well the 21cm data can constrain our free parameters. First, we consider the 21cm power spectrum data as shown in Figure 13 by itself, to see how tightly our parameters can be constrained by such observations alone. Then we add the 21cm data to our other existing observational constraints. In each case we use our MCMC framework to determine our best-fit values of our free parameters and their uncertainties using the entire data set, for the case of each telescope facility. This provides forecasting for how much improvement can be expected from future 21cm observations.

Figure 13 shows the 1D PDFs and 2D contours of our three parameters from the combined redshifts ($z = 9.0, 8.5, 8.0$) of 21cm mock observations by our three selected EoR experiments. To begin, we see that our MCMC search well recovers the best-fit input model (mock observation) parameters (black square points). This is to be expected, since this same input model was used to generate the 21cm data. The improvement to be noted here is the reduction of the uncertainties on these parameters relative to the previous case without 21cm data.

For LOFAR (green shaded area), we see that the 21cm

observations don't provide tight constraints due to large uncertainties as seen in figure 12. Essentially, mildly constraining the large-scale power provides little information on the ionisation sources that drive reionisation.

In contrast, HERA (blue) and SKA (red) provide quite tight constraints on the free parameters. Note that the scale of the posteriors is substantially reduced relative to our previous plots in order to enhance visibility. Hence future 21cm data alone can already independently constrain reionising sources, without adding in any other observations. Interestingly, there is almost no difference between the SKA and HERA constraints. This arises because the parameter constraints are predominantly driven by the larger scales, and HERA and SKA provide similar constraints on the power spectrum for scales $\gtrsim 2$ Mpc.

Comparing the 21cm constraints with constraints obtained from combining several EoR key observables, we find that constraining to 21cm observations yield smaller parameter errors. This can be clearly seen when comparing the $1-\sigma$ level of f_{esc} and A_{ion} found by constraining to the 21cm observations (fig 13) versus to the combined EoR sample (SFR, \dot{N}_{ion} , τ) (fig 11). However, it is evident that the 21cm future observation can constrain the f_{esc} tighter than the current EoR key observables.

In previous work by Greig & Mesinger (2015), the authors used a similar semi-numerical framework and performed similar analysis to constrain their free parameters to future 21cm mock observations. However, they did not have the photon escape fraction as a free parameter and rather constrained their efficiency parameter ζ , from which the f_{esc} can be computed for various assumptions about gas fraction in stars and ionising photons number per baryons (see their eq. (2)). However, we here constrain the f_{esc} directly without making further assumptions about the gas and baryons fractions, hence our presented f_{esc} results are direct, albeit the inherent photon conservation issues in these semi-numerical models, which we will discuss later.

We finally constrain our free parameters by combining the 21cm mock observations with the current EoR key observables (SFR, \dot{N}_{ion} , τ) as shown in figure 14. From this figure, we see that our three parameters are well-constrained by the combined set of current EoR and 21cm mock observations. Adding our combined EoR sample (SFR, \dot{N}_{ion} , τ) on top of the 21cm mock observations improves the error in estimating our free parameters, particularly for arrays with large 21cm errorbars such as LOFAR. This shows that the future 21cm observations are important in constraining the model astrophysical parameters and complement the other existing EoR various observations. A summary of our 21cm mock observations constraints combined with the other EoR observations is given in table 2.

Our 21cm forecasting shows that the future 21cm power spectrum observations will be crucial for providing tight constraints on various parameters related to the sources of reionisation. Even by themselves, such data will provide improve constraints over what can be obtained using current observations. When combined with other observations, the constraints get quite tight, even for the difficult-to-constrain photon escape fractions f_{esc} . The tightness of the constraints suggest that it may be possible to independently constrain variations in the escape fraction with mass or redshift; we will examine this in future work.

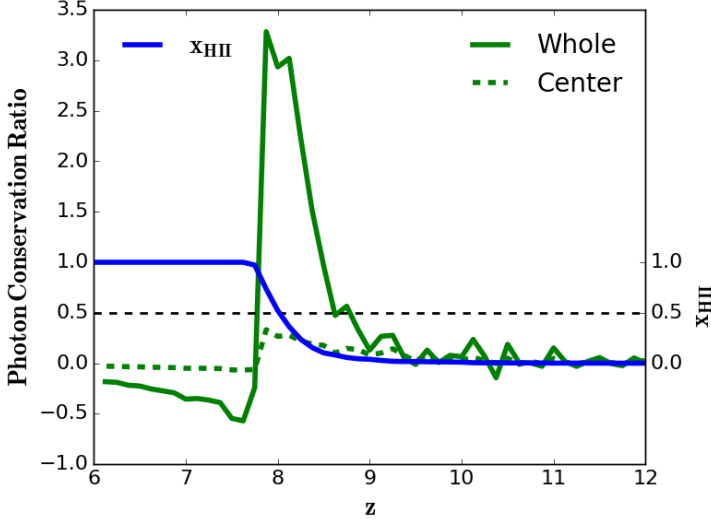


Figure 15. Photon conservation ratio from the Time-integrated EoR model using whole flagging (green solid) versus center flagging (green dashed) scheme, with their reionization history (blue solid). Horizontal black dashed line represents the 50% neutral/ionized fraction limit. Both methods violate the photons number conservations as seen by the under-ionization at high redshifts and over-ionization at end of reionization.

6.3 Photon conservation

To make use of our f_{esc} constraints, we here test the photon conservation problem in our semi-numerical model. Previous semi-numerical models, based on the excursion set formalism, have pointed out a violation in the photon number conservation. In Zahn et al (2007), the authors found that their semi-numerical model loses about 20% photons. They have argued that this photon loss arises from ionized bubbles overlapping, which they compensated by boosting the efficiency parameter ζ . More recent work by Paranjape et al. (2016) have developed a Monte Carlo Model of bubble growth to resolve the photon conservation problem in their semi-numerical model. Although their bubble growth model didn't resolve the problem completely, nevertheless improvements have been achieved and they have demonstrated that the problem comes from the fact that the excursion set-based models use the average mass of the bubbles rather than tracking the actual mass of sources and bubble local density fluctuations.

However, there are two methods to flag the spherical regions as ionized in the excursion set-formalism. The first is to flag the whole cells in the bubble (whole flagging) whereas the second is to flag only the center cell of the bubble (center flagging). We next use these two methods to verify the photon conservation in our Time-integrated EoR model. We would expect that, during time interval dt , the total number of escaped ionizing photons ($f_{\text{esc}} R_{\text{ion}} dt$) minus the total number of recombinations ($R_{\text{rec}} dt$) should be equal to the number of ionizations in the neutral hydrogen atoms ($(x_{\text{HII}}(t_{i+1}) - x_{\text{HII}}(t_i))N_{\text{H}}$). In other words, the successful photons that manage to escape from the interstellar medium (corrected by f_{esc}) and from high density regions along the way (subtracted by $R_{\text{rec}} dt$) should be equal to the total number of neutral atoms that have been ionized during time

dt . We can write the photon conservation ratio as follows:

$$\text{Photon Conservation Ratio} = \frac{(x_{\text{HII}}(t_{i+1}) - x_{\text{HII}}(t_i))N_{\text{H}}}{(f_{\text{esc}} R_{\text{ion}} - R_{\text{rec}}) dt}, \quad (9)$$

where $dt = t_{i+1} - t_i$. This ratio should be equal to unity for an ideal photon conserving model. However, the ratio can be less than unity when the universe is highly ionized. We then apply this ratio to the two methods, whole flagging versus center flagging, to check the photon conservation problem in both. We note that center flagging scheme requires about 20% more ionising photons to match the reionization history obtained by whole flagging method. We then adjust the f_{esc} in two methods to reproduce identical reionization history (identical τ) while keeping other parameters fixed.

In figure 15, we plot the photon conservation ratio for the two methods, whole flagging (green solid line) and center flagging (green dashed line) with the reionization history (blue solid line). We find that the center flagging scheme under-uses photons during all reionization redshifts, even after reionization ($z < 8$), which might partly explain the need for higher f_{esc} with this method. The photon loss in the whole flagging scheme agrees qualitatively with center flagging at higher redshifts when the universe is almost neutral.

As reionization proceeds, the whole flagging starts to over-use photons and ionizes more neutral atoms than expected. The photon excess/loss in the two methods are clearly redshift dependent. In the center flagging method, the photon loss is by a factor of $\sim 3, 7, 20$ at $z = 7.75, 9.25, 11$ respectively. The whole flagging scheme shows photon loss (under-using photons) at high redshifts and photon excess (over-using photons) at the end of reionization. At high redshifts, the photon loss, in the whole flagging, is by a factor of $\sim 2, 4, 7$ at $z = 8.75, 9, 11$ respectively. This shows that, at high redshifts, the photon loss, in the whole flagging method, is less by a factor of $\sim 2, 3$ as compared with center flagging method. At $z = 8.5$ ($x_{\text{HII}} \sim 0.9$), the whole flagging method satisfies the photon conservation condition as the ratio becomes unity, but the ratio does not converge at unity afterwards. After this point, the whole flagging scheme starts to overuse photons increasingly by a large amount till the end of reionization. We find the photon excess is about 10% at $z = 8.4$ and 70% at $z = 7.75$ (end of reionization).

We note that all our EoR models adopts the whole flagging method. This shows that our constrained photon escape fractions f_{esc} are, in fact, over-estimated by the photon excess associated with the whole flagging method. All our previous f_{esc} estimations can be corrected and lowered by 10% up to 70% depending on redshifts. The photon loss/excess evolution in redshift suggests that the f_{esc} might be required to change with redshift in order to preserve photon number conservation as a temporary solution.

7 CONCLUSION

We have improved our SIMFAST21 semi-numerical code for computing the EoR on large scales by incorporating a more physically-motivated criterion for determining whether a region of space is ionised, as well as integrating our framework into a full MCMC parameter search framework so we can

forecast how well current and future observations can constrain the physical properties of the sources driving reionization.

We have calibrated our new model to various current observations of the EoR, namely the Bouwens et al. (2015) SFR observations, the Planck (2016) optical depth measurements, and the Becker & Bolton (2013) \dot{N}_{ion} data. We also compared our new EoR model to our previous EoR model in Hassan et al. (2016) in terms of their EoR history, H II bubble sizes, and 21cm power spectra. We further studied variations in the 21cm fluctuations produced by all possible variants of our ionization conditions.

We then presented a robust MCMC analysis to constrain our generalized source model's free parameters against current EoR observations. We used the well-calibrated EoR model to predict the 21cm power spectrum for the future EoR array experiments SKA, HERA, and LOFAR. We show how the future 21cm observations are important for complementing the existing EoR current observations in order to tightly estimate the astrophysical parameters of EoR sources.

Our key findings are as follows:

- The Time-integrated EoR model produces reionization that starts fairly late ($z \sim 12$) and ends very rapidly $z \sim 7.5$. Comparing to the Instantaneous EoR model, the Time-integrated EoR model reionizes the universe earlier by $\Delta z \sim 0.5$, as shown in figure 1. Although the reionization is not much delayed, the reionization history evolution (shape) is remarkably different due to implementing different ionisation condition in each model (equation 4 versus equation 5).

- The Time-integrated EoR model produces very large H II bubbles as compared with the Instantaneous EoR model, and fewer small bubbles. This difference is clearly shown in their evolving HI maps (figure 2) and the ionization field (figure 3).

- The Time-integrated EoR model produces a larger ionization field power spectrum on large scales by 1-1.2 orders of magnitude, and lower ionization field power spectrum on small scales by a factor of 2-3 as compared with the Instantaneous EoR model, at various stages of the EoR (Figure 4).

- Likewise, the Time-integrated EoR model yields a 21cm power spectrum that is higher by 1-1.2 order of magnitude on large scales, and by $\sim \times 1.2-1.5$ on small scales versus Instantaneous EoR model at various global neutral fractions (Figure 5).

- Comparing to a similar semi-numerical model by Kulkarni et al. (2016), the Time-integrated EoR model produces the same shape of the 21cm power spectrum particularly during the intermediate and final stages of the reionizations (Figure 5). There is a minor difference in the amplitude of the 21cm power spectrum due to using our $R_{\text{ion}}-R_{\text{rec}}$ versus the standard efficiency approach.

- By considering all possible combinations between the hydrogen atoms and recombination terms in the ionization condition, we showed that recombinations are subdominant in determining the 21cm power spectrum particularly on large scales (Figure 6). The 21cm power spectrum amplitude and shape are highly sensitive to accounting for the amount of and fluctuations in the neutral hydrogen density. This means semi-numerical models must carefully account

for the neutral hydrogen to robustly predict the expected 21cm signal.

- The Bouwens et al. (2015) SFR observations provide tight constraints on the ionizing emissivity amplitude A_{ion} and the slope of the $R_{\text{ion}}-M_h$ relation C_{ion} , but provide no constraint on the photon escape fraction f_{esc} (Figure 7).

- The recent Planck (2016) optical depth value $\tau = 0.058 \pm 0.012$ poorly constrains our model parameters (Figure 8). This can further be seen in Figure 9 in which changing the f_{esc} from 0.2-0.8, for fixed C_{ion} and A_{ion} values, results in $\tau = 0.058-0.071$ consistent with the 1- σ level of recent Planck (2016) measurements. Although the degeneracy level is high among these parameters, the data slightly prefers models with lower values of f_{esc} , A_{ion} and C_{ion} .

- Similar to the τ constraints, the Becker & Bolton (2013) \dot{N}_{ion} measurements at a post-reionization epoch ($z = 4.75$) poorly constrain our model parameters in the selected prior range, but there is also a mild tendency towards lower values f_{esc} , A_{ion} and C_{ion} (Figure 10).

- Combining all of SFR, τ and \dot{N}_{ion} together results in tighter parameter constraints, as seen in Figure 11. The A_{ion} and C_{ion} here follow the previous constraints by the SFR observations, but combining these measurements yields better escape fraction constraints of $f_{\text{esc}} = 0.25^{+0.26}_{-0.13}$, though still not very tight. The parameters determined directly from the full hydrodynamic simulations analysed in Hassan et al. (2016) are consistent with these constraints.

- Using the well-calibrated Time-integrated EoR model, we predict the 21cm power spectrum at different redshifts ($z = 9, 8.5, 8$) for several constructed radio array designs, namely SKA, HERA, and LOFAR (Figure 12). While LOFAR does not provide strong constraints except at the largest scales, future experiments will tightly constrain the 21cm power spectrum to smaller scales that can better constrain the reionising source population.

- Using the 21cm mock observations alone to constrain our model free parameters, our MCMC technique is able to recover perfectly the input model parameters for SKA and HERA as seen in figure 13, and these data by themselves can provide fairly tight constraints on all our astrophysical parameters.

- By adding current EoR observations (SFR, τ , \dot{N}_{ion}) to the 21cm mock observations, we find that all experiments recovers the input model parameter accurately and the parameters error are further improved. This illustrates how future 21cm observations can complement and substantially improve upon existing EoR observations in order to more tightly constrain the emissivity of EoR sources and their relationship to the underlying halo population.

- We find that photon conservation is sub-optimal owing to the way the excursion set formalism is generically implemented in current semi-numerical codes, including SIMFAST21. The root difficulty is that cells are treated as fully neutral or fully ionised, with no possibility of intermediate ionisation levels. While some tuning could be done to minimise the problem, a robust solution likely lies in replacing the excursion set-formalism with a proper photon-conserving radiative transfer approach. We leave this for future work.

The SIMFAST21-MCMC platform developed here will be applicable for a wide range of EoR forecasting science

cases. By robustly incorporating all the current observables within an MCMC framework and being able to straightforwardly incorporate new data, we are building the tools necessary to optimally connect future redshifted 21cm power spectrum from the EoR to physical quantities associated with the population of reionising sources. Such a framework can be used to explore and constrain exotic source populations such as mini-quasars or Population III stars, as well as to potentially extend to multi-tracer cross-correlation approaches. The most immediate hurdle will be to develop a more robust yet still fast radiative transfer method that conserves photons, so we can more reliably assess the obtained source population parameters. There is much exciting work to be done as we continue to prepare for the 21cm EoR era.

ACKNOWLEDGEMENTS

The authors acknowledge helpful discussions with Andrei Mesinger, Greig Bradley, Jonathan Zwart, Girish Kulkarni, Tirthankar Roy Choudhury, and Neal Katz. We thank Jonathan Pober for making his 21cmSense sensitivity code publicly available and helpful discussions and comments. We also thank Dan Foreman-Mackey for his excellent MCMC code EMCEE and visualisation package CORNER (Foreman-Mackey 2016). SH is supported by the Deutscher Akademischer Austauschdienst (DAAD) Foundation. RD and SH are supported by the South African Research Chairs Initiative and the South African National Research Foundation. MGS is supported by the South African Square Kilometre Array Project and National Research Foundation. This work was also supported by NASA grant NNX12AH86G. Part of this work was conducted at the Aspen Center for Physics, which is supported by National Science Foundation grant PHY-1066293. Computations were performed at the cluster “Baltasar-Sete-Sois”, supported by the DyBHo-256667 ERC Starting Grant, and the University of the Western Cape’s “Pumbaa” cluster.

REFERENCES

- Akeret J., Seehars S., Amara A., Refregier A., Csillaghy A., 2013, *Astronomy and Computing*, 2, 27
- Barkana, R. & Loeb, A. 2001, *Phys. Rep.*, 349, 125
- Bauer, A., Springel, V., Vogelsberger, M., Genel, S., Torrey, P., Sijacki, D., Nelson, D., Hernquist, L., 2015, *MNRAS*, 453, 3593.
- Beardsley, A. P., Morales, M. F., Lidz, A., Malloy, M., Sutter, P. M., 2015, *ApJ*, 800, 128.
- Becker, G. D., Bolton, J. S. 2013, *MNRAS*, 436, 1023
- Bouwens J. R., Illingworth D. G., Oesch A. P., Trenti M., Labé I., Bradley L., Carollo M., Van Dokkum G. P., Gonzalez V., Holwerda B., Franx M., Spitler L., Smit R., Magee D., 2015, *ApJ*, 803, 34.
- Bouwens, R. J., Illingworth, G. D., Oesch, P. A., et al., 2015, *ApJ*, 811, 140,
- Choudhury T. R., Haehnelt M. G., Regan J., 2009, *MNRAS*, 394, 960
- Davé, R., Katz, N., Oppenheimer, B. D., Kollmeier, J. A., Weinberg, D. H. 2013, *MNRAS*, 434, 2645
- Dewdney P. E., 2013, Technical report, SKA1 SYSTEM BASELINE DESIGN.
- Ewall-Wice, A. et al, 2016, *MNRAS*, 460, 4320
- Fan, X., Carilli, C.L., Keating B. 2006, *Annual Review of Astronomy and Astrophysics*, 44, 415
- Feroz, F., Hobson, M. P., Bridges, M., 2009, *MNRAS*, 398, 1601.
- Finlator, K. Özel, F. & Davé, R. 2009, *MNRAS*, 393, 1090
- Finlator, K., Davé, R., Özel, F. 2011, 743, 169
- Finlator, Kristian; Muoz, Joseph A.; Oppenheimer, B. D.; Oh, S. Peng; Özel, F. & Davé, 2013, *MNRAS*, 436, 1818
- Finlator, K., Thompson, R., Huang, S., Davé, R., Zackrisson, E., Oppenheimer, B. D. 2015, *MNRAS*, 447, 2526
- Foreman-Mackey D., Hogg D. W., Lang D., Goodman J., 2013, *PASP*, 125, 306
- Foreman-Mackey, D., 2016, *JOSS*, 24.
- Gnedin, N. Y. 2000, *ApJ*, 542, 535
- Gnedin, N. Y., 2014, *ApJ*, 793, 29.
- Greig, B.; Mesinger, A., 2015, *MNRAS*, 449, 4246.
- Greig, B.; Mesinger, A., 2016, *arXiv:1605.05374*
- Hassan, S. and Davé, R. and Finlator, K. and Santos, M. G., 2016, *MNRAS*, 457, 1550
- Hinshaw, G. et al. 2013, *ApJS*, 208, 19
- Iliev, I. T., Mellema, G., Ahn, K., et al. 2014, *MNRAS*, 439, 725
- Iliev, Ilian T.; Santos, Mario G.; Mesinger, Andrei; Majumdar, Suman; Mellema, Garrelt; 2015 *Proc. Sci.*, Epoch of Reionization modelling and simulations for SKA. SISSA, Trieste, PoS (AASKA14) 007.
- Jensen, H. et al, 2013, *MNRAS*, 435, 460.
- Katz, H, Kimm, T., Sijacki, D., Haehnelt, M., 2016, *arXiv:1612.01786*.
- Keating, L. C., Haehnelt, M. G., Becker, G. D., Bolton, J. S., 2014, *MNRAS*, 438, 1820.
- Kulkarni, G., Choudhury, T. R., Puchwein, E., Haehnelt, M. G., 2016, *MNRAS*, 463, 2583.
- Majumdar S., Mellema G., Datta K. K., Jensen H., Choudhury T. R., Bharadwaj S., Friedrich M. M., 2014, *ArXiv e-prints*, *arXiv:1403.0941*
- Mesinger A., Furlanetto S., 2007, *ApJ*, 669, 663
- Mesinger, A.; Furlanetto, S.; Cen, R. 2011, 411, 955.
- Mitra, S., Choudhury T. R., Ferrara A., 2011, *MNRAS*, 413, 1569.
- Mitra, S., Choudhury T. R., Ferrara A., 2012, *MNRAS*, 419, 1480.
- Mitra, S., Ferrara, A., & Choudhury, T. R. 2013, *MNRAS*, 428, L1
- Mitra S, Choudhury T. R., Ferrara A. 2015, *arXiv:1505.05507*
- Mellema, G., Iliev, I. T., Pen, U.-L., & Shapiro, P. R. 2006, *MNRAS*, 372, 679
- McQuinn, M., Lidz, A., Zahn, O., et al. 2007, *MNRAS*, 377, 1043
- Paranjape, A., Choudhury, T. R., Padmanabhan, H., 2016, *MNRAS*, 460, 1801.
- Parsons, A., Pober, J., McQuinn, M., Jacobs, D., Aguirre, J., 2012, *ApJ*, 753, 81.
- Pawlik, A. H.; Schaye, J., 2008, *MNRAS*, 389, 651
- Pentericci, L. et al. 2014, *ApJ*, 793, 113
- Pober, J. C., Parsons, A. R. et al, 2013, *AJ*, 145, 65.
- Pober, J. C., Liu, A. et al, 2014, *ApJ*, 782, 66.
- Razoumov, A. O., Norman, M. L., Abel, T., & Scott, D. 2002, *ApJ*, 572, 695

- Planck Collaboration XIII, Ade, P. A. R., Aghanim, N., et al. 2015, arXiv:1502.01589 [PC15]
- Planck intermediate results. XLVII, Adam, R., Aghanim, N., et al 2016, arXiv:1605.03507
- Santos M. G., Ferramacho L., Silva M. B., Amblard A., Cooray A. 2010, MNRAS, 406, 2421
- Sobacchi E., Mesinger A., 2014, MNRAS, 440, 1662
- Schaerer, D. 2003, A&A, 397, 527
- Thomas, R. M., Zaroubi, S., Ciardi, B., et al. 2009, MNRAS, 393, 32
- van Haarlem, M. P. et al, 2013, A&A, 556, 2.
- Zel'Dovich Y. B., 1970, A&A, 5, 84
- Zahn O., Lidz A., McQuinn M., Dutta S., Hernquist L., Zaldarriaga M., Furlanetto S. R., 2007, ApJ, 654, 12
- Zahn O., Mesinger A., McQuinn M., Trac H., Cen R., Hernquist L. E., 2011, MNRAS, 414, 727